Evaluations on the Durability of Magnesia Magnesium Aluminate (MMA) Solid Oxide Fuel Cell Materials

Alexander James Stark

A thesis
submitted in partial fulfillment of the
requirements for the degree of

Master of Science

University of Washington
2018

Committee:
Dwayne Arola
Mark Tuttle
George Mayer
Brian Flinn

Program Authorized to Offer Degree:
Materials Science and Engineering

University of Washington

Abstract

Evaluations on the Durability of Magnesia Magnesium Aluminate (MMA) Solid Oxide Fuel Cell Materials

Alexander James Stark

Chair of the Supervisory Committee:
Associate Professor, Dwayne Arola
Materials Science and Engineering

Solid oxide fuel cells (SOFCs) are one of the most promising candidates for generating clean energy. Also known as "all ceramic" fuel cells, SOFCs use a range of advanced ceramic components to achieve the functionality that is required to attain high levels of efficiency, which exceed most other types of fuel cell systems. However, SOFC systems operate at high temperatures (500-1000°C). Therefore, the mechanical reliability and service life of advanced ceramic components has become "*the*" important area of research in this industry. Specifically, the static and dynamic mechanical integrity of these components under fuel environments at room and operating temperatures need to be investigated. To design viable commercial fuel cell assemblies, a comprehensive understanding of the mechanical behavior of the cells under the operating conditions is critical, and a qualification of the vendor components is essential. Flaws resulting from the manufacturing process, or that are introduced during handling and assembly, can cause a reduction in the strength of the cells as well as degrade their reliability. That requires a statistical approach for characterizing the mechanical properties of fuel cell materials and an understanding of the strength distribution rather than a deterministic definition.

In this investigation, the strength distributions of dense and porous Magnesia Magnesium Aluminate (MMA) candidate cell materials are evaluated under a range of environments, including exposure to hydrogen, nitrogen and moisture under elevated temperatures. Using this data, the slow crack growth behavior of the materials is characterized, and a fractographic analysis was performed on the component fracture surfaces to identify the origins of failure. The Mode I fracture toughness of the MMA is also evaluated at low (50°C) and elevated temperature (850°C) within a moist environment. It was found that the MMA exhibits a Weibull modulus of approximately 20, with limited differences between room temperature and 850°C, and that the strength exhibits very limited rate dependence, indicating low susceptibility to failures attributed to slow crack growth at these two temperature conditions. However, evaluations of the dense MMA at 50°C showed much greater SCG dependence, with an exponent of 29. Failures often initiated at surface pores that were introduced during the manufacturing process, which could serve as the limiting factor in commercial systems. The fracture toughness was not dependent on temperature, with the overall average value of 1.78 ±0.06 MPa•m$^{1/2}$. Results of this investigation contribute to the development of a comprehensive understanding of the structural behavior of MMA fuel cell materials, and will be instrumental in the choice of materials and manufacturing of reliable commercial systems.

Acknowledgements

I would like to thank LG Fuel Cell Systems for the opportunity to be a part of this research. Without the funding provided by the Department of Energy, this project would not have been possible. Thank you to Dr. Amit Pandey at LG for providing project insight and guidance. I would also like to thank my advisor, Professor Dwayne Arola, for his mentorship and support during the project and the writing process. I learned a lot from my time working with him.

To my parents, thank you for your never-ending support and encouragement, it has helped me to push towards greater goals and overcome challenges. And lastly, I would like to thank my girlfriend, Shreya Rajsekar, for her constant support and kind words. I don’t know where I would be without you.

Table of Contents

List of Figures

List of Tables

Chapter 1 - Introduction

1.1 Solid Oxide Fuel Cells

As the world moves toward sustainable and environmentally friendly techniques for power generation, fuel cells have received attention as a viable option. Efficient use of fuels as well as greatly reduced emissions are significant factors supporting the implementation of fuel cell technology. Although the concept of the fuel cell has been known for decades, limitations related to materials and efficiency have prevented large-scale adoption [1, 2]. Through extensive research and scientific focus over the last several years, materials have been developed which allow for fully functional and effective fuel cells [3]. One type of cell, namely the solid oxide fuel cell (SOFC), has been especially challenging due to its required high temperatures of operation [4].

SOFCs are distinct from other cells as they utilize a solid electrolyte material as opposed to liquid electrolytes. Due to the high efficiency under certain conditions of operation, which can exceed 70%, SOFCs are highly promising and cost-effective candidates for power generation [3, 5]. This statement is especially true when they are paired with other systems to take advantage of waste heat [5]. However, limitations associated with the materials and manufacturing costs have slowed progress in their development. As such, most current research has been devoted to engineering new material options, finding ways to reduce operating temperatures, and lowering production costs [6].

1.2 Operation

The operation of SOFCs is quite simple as there are only three main components involved in their function, which include the anode, the cathode and electrolyte. The general structure involves an electrolyte sandwiched between the anode and cathode layers as shown in Figure 1.1.

Both the anode and cathode are porous whereas the electrolyte is non-porous as dictated by their various functions [3]. The cathode side is exposed to an air mixture containing O_2, while the anode side is exposed to the specific fuel to be used. As the O_2 passes through the cathode it is reduced to oxygen ions, which then come into contact with the electrolyte. The electrolyte is typically a stable ceramic, which allows for the transport of oxygen ions. The transport process follows ionic diffusion mechanisms and is driven by a concentration gradient of oxygen ions through the layer [5]. At the same time, fuel is being transported through the anode to the anode/electrolyte interface. As the fuel is oxidized by the oxygen ions at the interface, a reaction takes place that generates electric current [5, 6]. In addition to electricity, other products are released such as water, heat and small amounts of other fuel byproducts. As electrons are released, they are channeled through an electrical circuit that contributes to the generation of power.

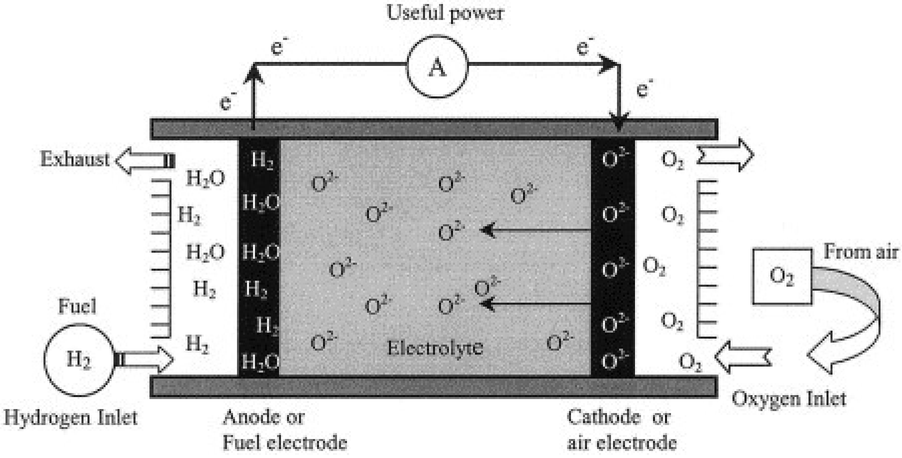

Figure 1.1: Schematic diagram of a solid oxide fuel cell with its main components, namely the anode, cathode and electrolyte. Taken from *[5]*.

Due to a number of advantages, SOFCs have the potential to become one of the primary methods for clean power generation, but there are presently a number of challenges facing this technology [7]. One of the main advantages of SOFCs is the flexibility in fuels that they can tolerate. Where other types of cells require high refinement of supply fuels to prevent degradation of cell materials, the solid oxide fuel cell can utilize a wider range of fuels without the need for expensive refinement processes [6]. Some of the most common fuel types include hydrogen, natural gas and methane [8]. This capability is attributed to the high operating temperatures required for the ion transport mechanisms to reach an effective level. Unfortunately, the high operating temperature is also the biggest disadvantage to SOFCs. First and foremost, extreme temperatures in the range of 600° to 1000°C impose major limitations to the materials available for use [1, 9]. Each fuel cell component must be robust enough to maintain its performance over the entire range of operating conditions it is exposed to, and over the desired lifespan of the cell. It is well established in this industry that material properties are not necessarily constant as particular aspects of their environment change. Since the anode, cathode and electrolyte are bonded together, it is critical that they have similar coefficients of thermal expansion (CTE) to prevent damage from taking place during temperature cycles. Perhaps the primary difficulty that arises from high temperature operation is the extent of thermal expansion in each material as well as the differences between those with different CTEs. If the materials expand to a different extent, thermal stresses can develop, which leads to bond failure and loss of fuel, or mechanical failure in other components of the cell [2, 9, 10, 11].

1.3 Fuel Cell Assembly and Concerns

Solid oxide fuel cell systems achieve high energy densities by stacking a large number of individual fuel cells together. A few images of the cell stacks from a major manufacturer in the US are presented in Figure 1.2. The image on the left shows a set of individual cells stacked in five columns and this assembly is then placed inside an enclosure (right) where fuel is delivered via inlet hoses. As a result of this stacked configuration and large number of parts, these systems require a significant analysis of the reliability to prevent unexpected failures and the need for costly service.

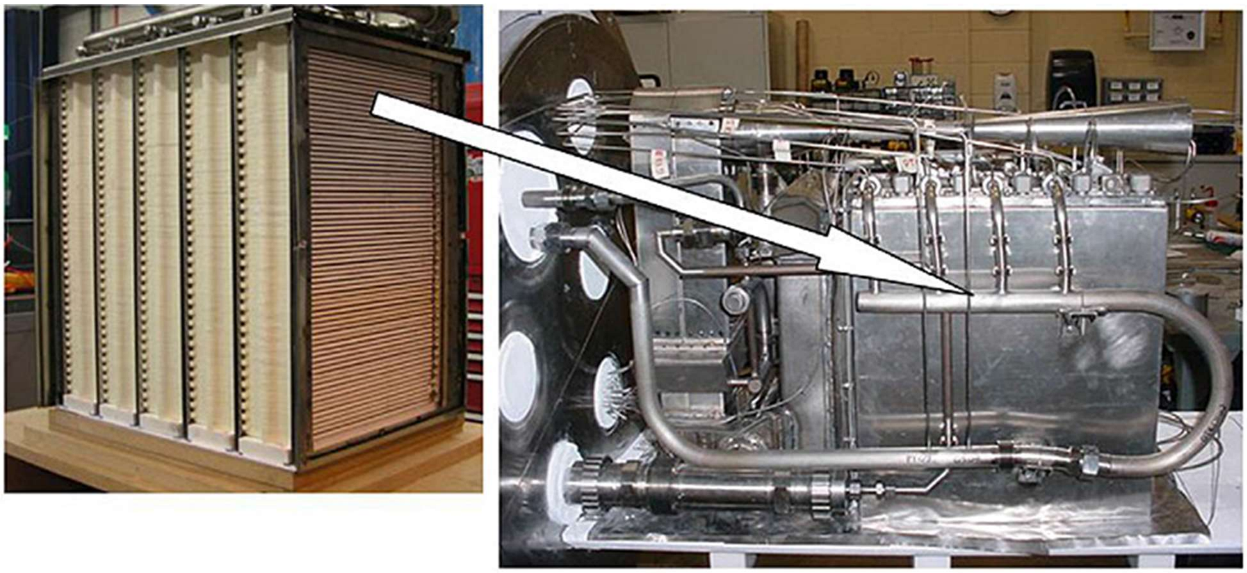

Figure 1.2: Solid Oxide Fuel Cell assemblies: Left - An example of multiple fuel cells stacked together. Right – An assembly where fuels are delivered to cells. Images courtesy of LGFCS.

From the images in Figure 1.2, it becomes apparent that there are hundreds of individual cells; each one of which could experience a mechanical failure. Due to the complexity of these intricate assemblies, the failure of even one component of the assembly is substantially detrimental as repair or replacement requires a significant amount of both time and effort. Clearly, a detailed evaluation of the mechanical behavior of the fuel cell materials and their reliability is essential for long-term implementation of SOFCs. If a cell stack can be designed for multiple years of operation with an acceptably low probability of failure, expensive repairs can be avoided.

There are several factors that can be detrimental to the reliability of SOFC systems, which can be broken down into three main groups: i) thermal stresses, ii) residual stresses and iii) manufacturing defects. Due to high temperature operations, thermal stresses are perhaps the primary contributor to reduced material lifetimes and pose the greatest potential for sudden failures [9]. Thermal stresses can be imposed on the cell stack for several reasons, one being a non-steady temperature level [10, 12]. As with any power generation source, a SOFC stack can undergo a potential operation error that causes an unexpected system shut down. During these scenarios, there is a sudden reduction of temperature which will lead to uncontrolled contraction of various components. As mentioned previously, any CTE mismatch between cell components can cause the introduction of stresses with extreme temperature changes such as a cell stack shutdown. An example of a particular region of interest is presented in Figure 1.3, which shows a magnified image of a few fuel cells that are stacked together in a multiple-cell structure. Also visible are bonded joints between specific components of the assembly. This bonded joint includes dense end-caps and porous tubes that are bonded together using a glass-ceramic.

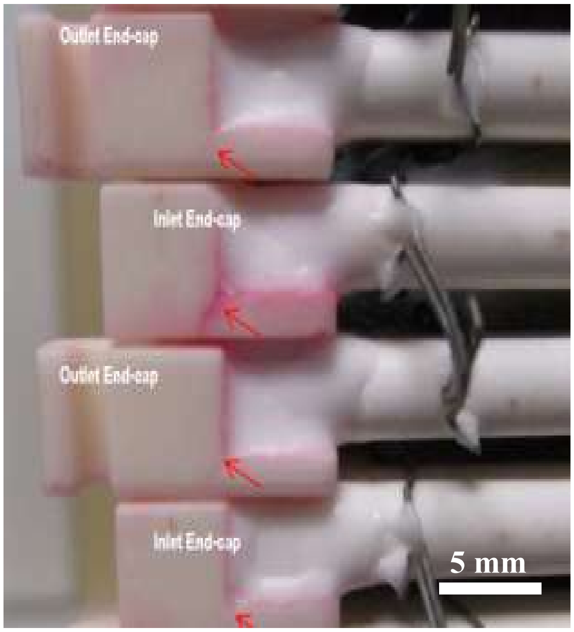

Figure 1.3: Close-up view of solid oxide fuel cell components stacked together. The pink coloration is a tone created by a highlighting process used to accentuate defects. The arrows point to cracks which have developed at the intersection of dense and porous components, and reside at a region of stress concentration within the end caps of dense ceramic components. Photo is courtesy of Dr. Amit Pandey, LG Fuel Cell Systems.

These bonded joints are highly susceptible to failure under thermal stresses and de-bonding may occur if the thermal stresses become too great [13]. In addition, these joints include sharp corners that promote stress concentrations. They are at risk for the development of cracks, which may cause immediate failure through loss of fuel or severely weaken the cell structure enough to result in mechanical failure. Events of that type will cause a significant reduction in the expected life. In a similar manner to changes in temperature due to operation cycles, temperature gradients may develop across different regions of individual cells as well as the cell stack. Temperature gradients give rise to thermal stresses within the cell materials and could lead to the formation of cracks, or the growth of existing cracks like those shown in Figure 1.3 [10]. The greatest concern is that damage of this type could lead to premature component or system failure.

Another source of concern within SOFC components is residual stress. Residual stresses can be described as stresses present in a material which remain after all external forces have been removed [14]. These stresses are often within the material as a result of the manufacturing process and as a consequence of either non-uniform thermal or mechanical stresses beyond the elastic limit [15, 16]. Residual stresses are of concern in SOFC materials [17]. One area where this type of stress can pose a tremendous problem is within joints or bonded locations that experience a static stress as a result of the assembly and the CTE mismatch. Residual stresses are extremely detrimental within ceramic components, relative to metals, due to the fact that they are brittle materials [18]. The manufacture of ceramic components is typically achieved via a multitude of steps that involves the consolidation and sintering of ceramic particles [19]. The compaction and sintering process can impart either tensile or compressive residual stresses [15]. In this particular process, the residual stresses can develop due to non-uniform particle density distributions, and corresponding non-uniform thermal distributions during sintering [15, 20]. Residual stresses can also be introduced through processes performed to achieve final net shape such as grinding or other finishing operations. This leads to the third major consideration for reliability, i.e. manufacturing and defects.

Manufacturing often involves changes in the phase of materials, changes in microstructure and of course, changes in shape. The processes required to achieve these changes are subject to variations that can lead to defects. Defects can take many forms and range from the micro-scale with lattice imperfections up to macro-scale with large pores and foreign particulates. The types of defects are dependent on the materials and the processes they are subjected to. Of primary concern, deviations or discontinuities in the microstructure could result in a change in mechanical behavior. Voids and large foreign particles in the form of inclusions can promote stress concentrations and cause a reduction in strength and reliability [21]. Other types of flaws can be introduced via external sources like machining and grinding. These processes can result in a surface texture that poses surface stress concentrations, or promote the development of residual stresses due to the non-uniform stress distribution applied to achieve localized material removal. Furthermore, machining can introduce damage such as chips and cracks in ceramic components [22, 23]. These types of defects are particularly detrimental due to the extreme surface flaw sensitivity of brittle ceramics. For example, Allor and Baker [24] evaluated the importance of surface grinding conditions on the strength distribution of hot pressed silicon nitride (HPSN) ceramics as shown in Figure 1.4. In this particular figure, the strength distribution is presented for four different types of grinding operations that involved variations in direction and cutting type [24]. The results of grinding were evaluated in terms of the strength distributions, and adopted Weibull distributions to characterize the importance of the methods of surface preparation.

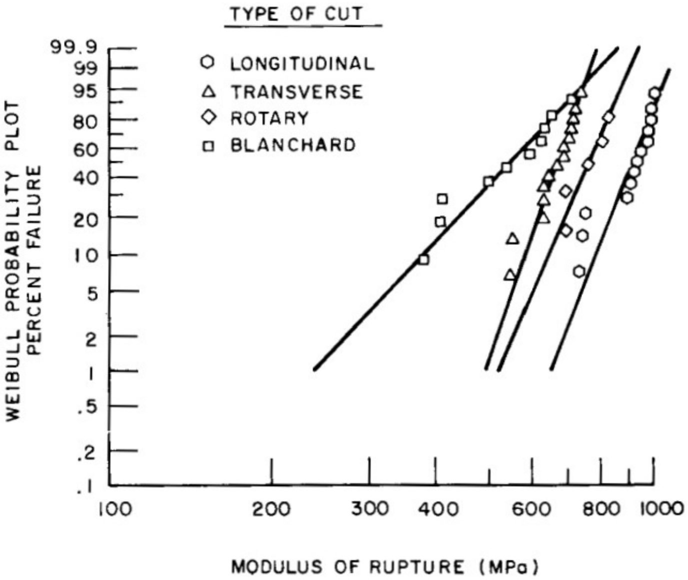

Figure 1.4: The effects different grinding operations have on the strength distribution of a HPSN ceramic presented in terms of a Weibull plot. The data presented in this figure is from *[24]*.

Results of that study showed that grinding transverse to the longitudinal direction of the component and corresponding direction of maximum principle stress resulted in a reduction in the strength of the material. This reduction is due to the differences in orientation of the peaks and valleys of the surface texture and the extent of stress concentration they pose. Perhaps of greater degradation, grinding with larger abrasive particle sizes was also found to result in a substantial reduction to the material strength [24, 25].

Based on the aforementioned description, the strength and reliability of SOFC components can be dependent on intrinsic and extrinsic qualities of the components. The intrinsic factors involve those that are based on the chemical composition and the strength of the ionic and covalent bonds of the ceramic. The extrinsic factors involve the plethora of deleterious features that can be introduced as a result of the manufacturing processes, as well as those that may result as a function of the environmental exposure. Through a detailed evaluation involving precise control of the manufacturing process and the environmental conditions used for evaluating the materials, the most detrimental aspects of the materials and processing can be identified and changes implemented to mitigate the problem. For example, if components in a SOFC assembly are identified to exhibit inferior strength distributions due to significant levels of porosity, then the company can work with the manufacturer of the components to modify the processing techniques and achieve lower porosity levels. This procedure involving testing and evaluation is the purpose of the research described in this thesis. The results of this work will be used to assist in the development of valid candidate materials for a particular commercial fuel cell assembly and the environmental conditions that are responsible for degradation.

1.4 Mechanical Evaluation of Ceramics for SOFCs

As previously described, SOFCs are constructed of ceramic materials as there are no other materials that can survive the elevated temperature conditions that are required for their function. Ceramics offer many advantages such as low thermal and electrical conductivity as well as their maintained strength at elevated temperatures, all of which are essential for fuel cell operation [26]. In some cases, a ceramic substrate is used as the structural support in the cell design. Although this design choice makes sense for many reasons, ceramics are typically very brittle materials [26], which is a critical concern and perhaps the Achilles heel of SOFCs.

The major implication of their brittle nature is, by definition, their low strain to fracture and limited tolerance to defects and flaws. As such, brittle materials pose a risk as there is very little warning before catastrophic failures which can originate from defects that are a result of the manufacturing process or assembly. Thus, based on the extreme operating conditions of SOFCs, it is essential to understand their strength distribution in a manner that establishes the effects of existing flaws, and that accounts for potential changes in mechanical behavior with prolonged service. A deterministic definition of strength is not adequate for these brittle, highly flaw-sensitive materials.

Failures in ceramics can be the result of a range of factors which are influenced by how the material is manufactured. Due to the fact that they remain linear elastic to failure, surface and internal flaws are detrimental as they create a stress concentration or stress intensity that does not decreases as a result of inelastic deformation. Flaws can take the form of foreign particulates, in the form of pores or voids, or defects introduced by poor tools and forming [27]. Discontinuities within the material structure act as stress concentrations, reducing the overall strength and reliability [27]. The distribution of flaws within one region of a component or within one component relative to others are not always consistent. Therefore, the strength of one component can vary drastically from another [28]. To obtain a reliable measure of the failure strength of these materials, it is necessary to test a large number of samples to obtain an understanding of the strength distribution.

Due largely to the difficulties encountered in manufacturing, the primary structural component in SOFC systems is a ceramic substrate with planar or tubular form [5]. Through mechanical evaluations of the substrate, it is possible to assess the expected performance in different operating environments. Using that data, it is possible to evaluate whether that material is a viable option for use in a specific fuel cell design or to use the distribution in data to define the design in terms of the probability of failures. There are several options for evaluating the mechanical behavior of ceramics, and one of the most accepted methods is flexural testing [29]. In fact, flexural tests are also particularly relevant for fuel cell materials as bending stresses are commonly introduced to the components during operation [30, 31].

Flexure testing of ceramic materials should be conducted according to appropriate standard methods of evaluation. The most common method for flexure testing of ceramic materials is ASTM C1161 [32]. According to this standard, the fixtures can be in either a 3 or 4-point bend configuration (Figure 1.5) depending on the purpose of the evaluation [32]. By varying the testing conditions and environment, a comprehensive view of the mechanical behavior can be achieved and utilized in design and analysis.

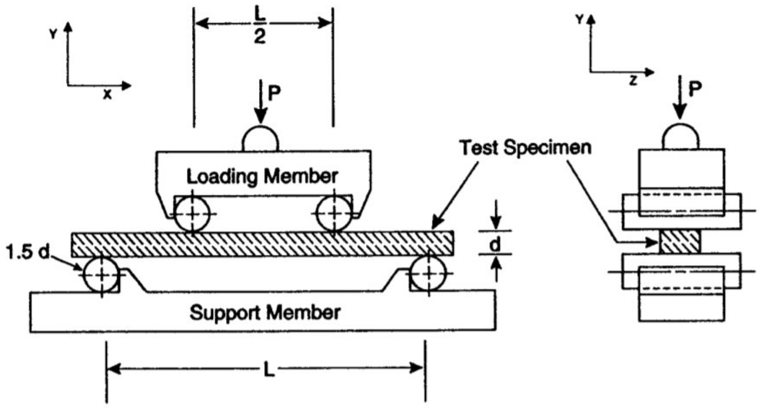

Figure 1.5: Schematic diagram of a standard 1/4 pt. 4-point bend fixture with a loaded test specimen. Diagram is from *[32]*.

One of the most appropriate ways to evaluate the strength distribution of a brittle material and to compare sets of data corresponding to different materials or evaluation conditions is to organize the data into a Weibull plot. Weibull statistics can be used to analyze the probability of a material failing based on an adequate number of data points [28, 30]. According to the Weibull weakest-link model, the probability of failure (P) for a material subjected to a level of stress (σ) is given by

$$P(\sigma) = 1 - e^{-\left(\sigma/\sigma_0\right)^m} \quad (1)$$

where m is the Weibull modulus and σ_0 is a scale parameter. This equation assumes similar volumes and stress distributions between test samples [33]. By obtaining strength values for a set of constant-volume bars and converting them into a probability distribution, the Weibull parameters can be determined.

Two important parameters are defined in this treatment including the Weibull slope or shape parameter, and the Modulus of Rupture (MoR) [28, 33, 34]. When a set of strength measurements are plotted against their probability of occurrence, the distribution can be used to develop a Weibull model description for the response. An example of a Weibull plot for the strength distribution of a silicon nitride material is shown in Figure 1.6.

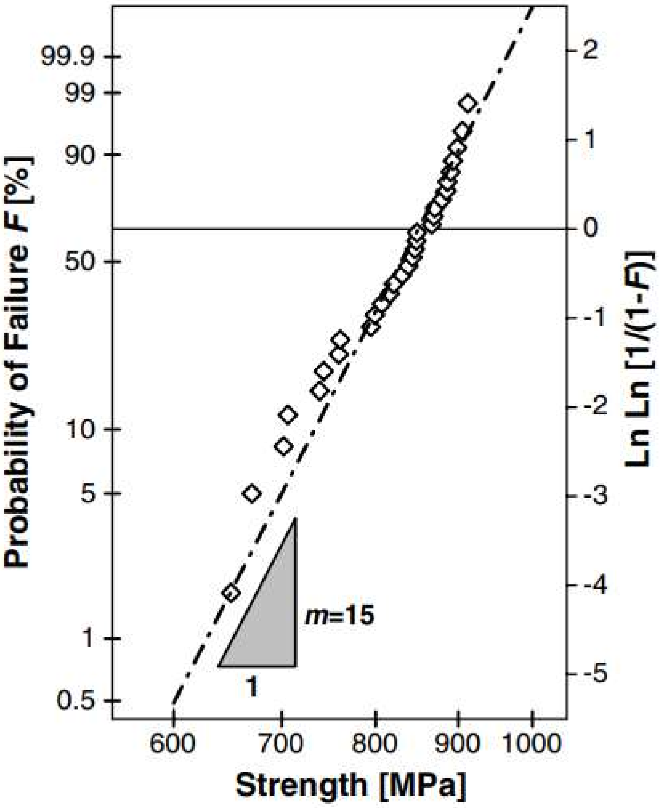

Figure 1.6: Sample Weibull plot for silicon nitride, which shows the slope of the trendline (Weibull modulus) and cross at the location of the MoR *[28]*.

In the graph presented in Figure 1.6, the measures of strength conform to a linear distribution when plotted in this manner. The slope of the data, i.e. the Weibull modulus, is of substantial importance as it is distinctly correlated with the flaw distribution [28, 30]. If the slope is high then it shows there is a small degree of variation in the strength measurements, implying that the flaws or defects serving as the weak link are highly consistent. A high slope is beneficial because it indicates that the strength of additional specimens or components can be estimated with a high degree of accuracy. The graph also shows that at higher levels of stress, the probability of failure increases to 100%. The modulus of rupture or characteristic strength is also beneficial for calculations and modelling as it provides a useful value where there is a 63.2% chance of failure. When evaluating the influence of different variables on the mechanical response of a material, Weibull plots can serve as a powerful approach to compare strength distributions. For example, if the Weibull slope decreases with an increase in environmental temperature without changes in the MoR, then the strength of the material becomes less predictable at higher temperatures. The Weibull distribution of data can help in material diagnostics.

1.5 Slow Crack Growth (SCG)

The operation of a SOFC leads to cell materials being exposed to a wide range of temperatures and chemical environments. One concern is the use of glasses and ceramics for structural applications is their sensitivity to slow crack growth or dynamic fatigue [35]. It is important to consider this aspect of material behavior in the analysis of the mechanical behavior and strength distribution of the ceramics for SOFCs.

Factors such as water, temperature and gas composition all play a role in influencing flaws and their growth over time [36]. In the study of glasses, small sub-critical cracks can grow under a quasi-static stress due to the corrosive nature of water at the crack tip [37]. The advancement of the crack, or the crack tip velocity, can be related to the stress intensity factor [38].

In ceramics, stress corrosion takes place when reactive molecules from the environment are able to react with and break bonds within the material structure. When stresses are applied, bonds at a crack tip are strained and are more susceptible to breakage, allowing for crack propagation at loads which are lower than those needed to reach the typical fracture toughness of the material [39]. Strained bonds are more likely to be broken due to a lowering of the required activation energy for bond breaking [39]. As an example, a simple zirconia or silicon oxide is susceptible to stress corrosion with water. When these oxide ceramics are in contact with water molecules, one hydrogen atom from the water can undergo bonding with the oxygen ions of the oxide bonds and the remaining hydroxide group bonds with the metal in the oxide bond. This process results in a severed oxide bond with two hydroxide groups in its place [40] and this reaction between ceramics and water is potentially detrimental to a wide range of oxides. Specifically, the materials attacked by this reaction can undergo crack extension under quasi-static stresses at levels of stress intensity that are less than that required for fracture. In the magnesium aluminate spinel phase of MMA, it is possible that the aluminum-oxygen bonds are susceptible to corrosive attack by water or hydrogen. Therefore, it would follow that locations rich in alumina content may be of highest concern in MMA. However, an investigation reported by Rice claims that while MgO does not show significant slow crack growth sensitivity, alumina does [41]. Static stresses applied to the materials as well as a high temperature environment allow these reactions to take place at the vicinity of the crack tip when they normally would not be possible. These factors have a direct impact on the effective stress intensity that enables crack growth to take place at the sub-critical flaws, and subsequently, the crack growth velocity [39].

The relationship between the crack growth velocity and the stress intensity in materials that experience SCG has been interpreted according to the diagram presented in Figure 1.7. As evident in this figure, the material response is divided into three major segments where different mechanisms dominate the crack velocity. Region I, which corresponds to near-threshold stress intensity ranges, is a reaction rate controlled state where the corrosive species are reacting at the crack tip and controlling its shape and extension. In this region, the crack tip velocity increases rapidly with increasing stress intensity. Region II is dominated by the rate of diffusion of the same species to the moving crack tip and is marked by little to no change in velocity as stress intensity is increased. Region III is the point at which fast fracture begins to occur and even small increases to stress intensity can cause failure.

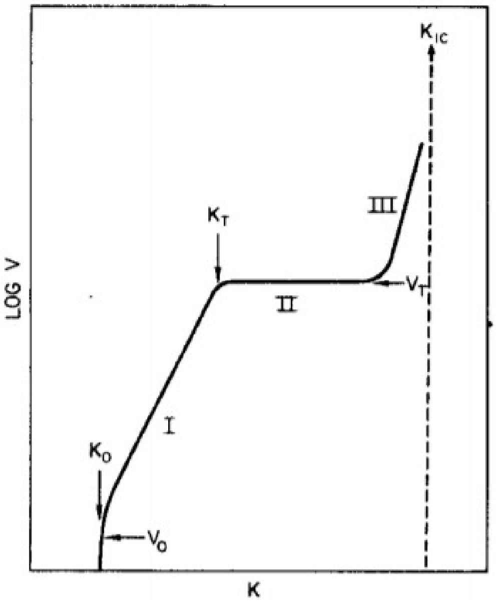

Figure 1.7: Relationship between crack tip velocity and stress intensity for stress corrosion. This graph is from *[38]*.

The degradation mechanisms responsible for SCG take time to evolve [35]. As such, the rate of loading, and the magnitude of a quasi-static loading posing a stress-intensity can result in significant differences in apparent strength of the material. If SCG is to be avoided in an evaluation of a specific material, then testing conditions that include high loading rates, use of an inert atmosphere and absence of moisture, or testing at low temperatures can be used to minimize the influence of the mechanisms of degradation [36]. This concept was tested by Rice for $MgAl_2O_4$ where strength evaluations were conducted at room temperature (22°C) and at a temperature of -196°C, obtained through the use of liquid nitrogen [41]. Rice found that strengths at the lower temperature were 20-30% higher than at room temperature. After accounting for the temperature dependence of Young's modulus, it was determined that the majority of this difference was due to a reduction in the activity of water molecules and hydrogen atoms at the low temperatures.

The material response under conditions that are susceptible to SCG is limited to the influence of the initial flaw distribution present in the material [30]. In cases where a stress is applied and promotes the development of a stress intensity at a crack tip, stress-corrosion can become activated, and can be further exacerbated by the environment which the material is exposed to [42]. If tests are conducted under high temperatures and environments with high levels of corrosive species, the mechanisms involved in stress corrosion can become more prominent and accelerated. For SOFC materials exposed to such concerning environments, it becomes necessary to determine whether SCG is present and to what extent.

Due to the mechanisms of slow crack growth, particular attention must be placed on the material surfaces and the types of flaws that are present. Surface defects and pores act as stress concentrators, but they also can increase the susceptibility to SCG. Indeed, Charles and Hillig developed a model to describe crack velocity based on the idea that the geometry of surface defects in a brittle material are altered by the corrosion mechanisms outlined previously [43]. In addition to defects introduced during manufacturing, there may be other unexpected damage from assembly and service. For example, as evident from Figure 1.3 cracks can develop in regions susceptible to stress, even before the components are placed in service. These types of cracks provide another point of attack for corrosive environments and are a cause for major concern in environments that promote SCG. In many cases, these cracks will already have sharp tips which allow for propagation under smaller loads due to their higher level of stress intensity. Due to these concerns, testing for the influence of different environments, particularly those containing moisture and hydrogen, is required to obtain confidence in material performance and durability.

1.6 Objectives

The primary objective of this research is to evaluate the durability and reliability of a candidate Magnesia Magnesium Aluminate (MMA) material for dense and porous components of commercial SOFCs. Due to the potential changes in mechanical behavior and fracture resistance of fuel cell materials under the service conditions associated with power generation, and the potential for SCG to be a contributor, it is essential to perform evaluations that closely mimic typical solid oxide fuel cell operating conditions. Thus, this investigation will consist of the following four specific aims:

1. Develop a testing arrangement that supports experimental evaluation of the flexure response of dense and porous MMA materials under elevated temperature (up to 1000°C) and that enables control of the moisture content and the development of specific chemical environments that are of interest to explore.
2. Utilize the new experimental arrangement to perform flexure tests on both dense and porous MMA materials according to ASTM standard C1161 [32]. These tests will enable a determination of the strength and strength distributions over a wide range of loading rates as well as enable a determination of material reliability. The results of this quantitative analysis will be complimented with a fractographic evaluation of the fracture surfaces to determine the primary defects and origins of failure.

3. Evaluate the slow crack growth responses of the MMA according to ASTM C1368 [44] under the flexural loading format and under specific environments and temperatures specified by the contracting organization. This aspect of the evaluation will be used to understand the importance of stress rate to the fracture resistance of the MMA material and the contribution of the reformat fuel environments to the mechanical behavior.

4. Porosity is present within ceramic materials, including the MMA. Therefore, it will be beneficial to examine the influence porosity levels have on mechanical behavior. Through the examination of both dense and porous MMA, it is hoped that a relationship can be developed between the porosity level and the corresponding mechanical behavior. Although the strength of structural ceramics benefits from limited porosity, some levels of internal pores may be acceptable with specific definitions of probability of failure.

As a supplement to the aforementioned specific aims, additional properties are determined that are identified to be useful in the implementation of the MMA material. For example, estimates of the fracture toughness will be pursued as well as a comparison of the strength distribution with respect to other candidate ceramics. This information will be useful to develop further understanding of the relative benefits of MMA in the SOFC industry and to provide feedback to suppliers which enables them to improve their manufacturing process and overall product.

Chapter 2 - Materials and Methods

2.1 Material Details

The materials in this evaluation consisted of dense and porous components of the solid oxide fuel cells under development by LG Fuel Cell Systems (LGFCS) of Canton Ohio. An example of a complete single fuel cell is shown in Figure 2.1. The strength distribution of both the dense end cap material and the porous tubes were evaluated.

Figure 2.1: Picture of a complete single fuel cell. Areas marked with the number 1 are dense end caps and areas marked with the number 2 are porous tubes.

The materials for both the dense and porous components were Magnesia Magnesium Aluminate (MMA), with 38% alumina by weight. The phase diagram of this material is listed in Figure 2.2. In the range of operating temperatures for SOFCs (from 20°C to nearly 1000°C), the material composition consists of both the spinel $MgAl_2O_4$ and magnesia (MgO) phase. A change of phase from that achieved by manufacturing does not take place.

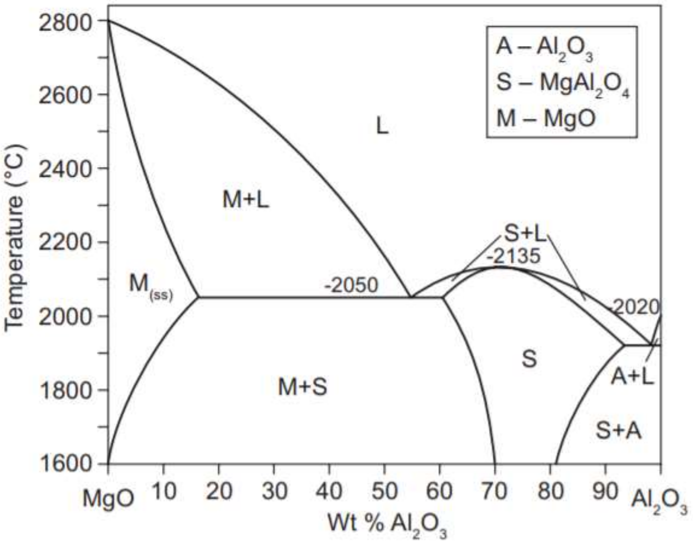

Figure 2.2: Phase diagram for MgO and Al2O3 *[45]*. This diagram illustrates that for the 38% alumina content of the MMA, the material consists of a MgO and $MgAl_2O_4$ spinel composition. In addition, over the range of temperatures evaluated in this investigation (approx. 20°C to 850°C) there is no change in phase.

2.2 Thin Dense MMA (38% Alumina Content)

Two different major batches of 38% dense MMA components were evaluated. The first batch of dense 38% MMA consisted of 150 individual components that were received in an as-manufactured state. To obtain a standardized sample for flexural testing, a 3 mm wide section of material was machined from the thin region as depicted in Figure 2.3. To perform these operations, the MMA components were bonded to a sheet of 1/8” thick glass, that was in-turn bonded to a steel plate. A stick of Crystalbond 509 clear color mounting adhesive was used as the bonding material. To mount the samples, the steel plate and glass sheet were placed on a hot plate and heated to a temperature of approximately 120°C for 10 minutes. A thin layer of Crystalbond was then applied to the glass surface by allowing the stick to contact the heated sheet of glass. Dense MMA components were then placed onto the glass surface with adhesive. Each component was gently moved side-to-side with downward pressure applied to ensure wetting of the entire contact surface and to allow for a thin and evenly distributed layer of adhesive. The mounting assembly sat on the hot plate for an additional 5 minutes before removal. The assembly was then cooled to room temperature where the bonding adhesive returned to solid state.

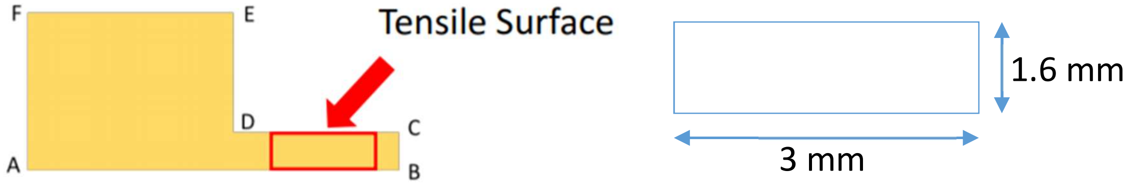

Figure 2.3: Details of the specimen preparations used for obtaining flexure specimens from the dense 38% MMA components. Left - geometry of a dense 38% MMA component as-manufactured with markings to indicate where samples were removed. Right – final geometry of the specimen.

The sectioning was completed through use of a Chevalier Smart-H818II surface grinder/slicer with a 0.46 mm thick, 150 mm diameter diamond cutting wheel with 320 mesh abrasives. To reduce cutting friction and heat, a continuous coolant was applied throughout the cutting procedure, which consisted of water with Rustlick WS-5050 cutting oil. Slingers with a diameter close to the diameter of the cutting wheel were used to control blade stability and improve final sample geometry. The plate with mounted samples was placed on the magnetic grinding surface with the long axis of the samples parallel to the cutting blade. Wheel surface speed was set such that 3000 RPM was achieved during the cutting procedure. Coarse grinding with a down-feed interval of 0.05 mm was used for the bulk of cutting, followed by fine grinding with a down-feed interval of 0.013 mm to finish the sectioning. The fine grinding was used as the blade approached the bottom of the component to reduce the potential for chipping damage. The x-axis feed rate was set to approximately 60 mm per minute. Two sections were made parallel to the length of the dense components (Figure 2.3) to obtain rectangular dense MMA samples with 3 mm width, 1.6 mm thickness and approximately 60 mm length. These specimens are not consistent with the geometry defined by ASTM standard C1161 [32] due to limitations posed by the component geometry.

Upon completion of the sectioning process, the mounting plate and samples were returned to the hot plate, the temperature was set to 120°C and the mounting assembly was heated for ~10 minutes. Each sample was removed from the glass plate with tweezers and placed on a paper towel. A majority of the liquid Crystalbond was wiped off with a cloth rag. Due to potential effects of moisture on the mechanical performance of the candidate materials, a drying phase was implemented immediately after the sectioning process. All of the evaluated materials went through a low temperature drying at 120°C for 2 hours. Thereafter, and prior to evaluating the mechanical behavior, an additional firing of the samples was completed at 1060°C for 2 hours. Any Crystalbond that remained on the samples was completely removed during the firing process. To remove sharp edges and potential defects after machining, a small 45-degree chamfer was introduced along the long edges of all samples. This was done by lightly rubbing the sample back and forth on a piece of 800 grit sandpaper 4-5 times per edge.

Flexural strength evaluations were performed on the dense 38% MMA according to ASTM C1161 [32]. Although this standard is specified for ambient conditions, it was used as a guide for testing under all conditions in this study, including those with elevated temperatures, with moisture and other chemical compositions. The slow crack growth response of the ceramics was determined according to ASTM C1368 [44], which defines both the methods of testing and for determining the slow crack growth parameters of advanced ceramics by constant stress-rate flexural testing. All tests were conducted with a ¼ point 4-point bend fixture made of high purity alumina that had an inner and outer span of 20 mm and 40 mm, respectively, as shown in Figure 2.4. The rollers were free to articulate to accommodate for test sample deflection and minimize interface friction. A loading ball was used to apply load to the upper fixture to ensure proper alignment during testing. All testing was conducted with a commercial universal testing frame (Instron Electropuls E1000, Norwood MA, USA) with the capability of accurately controlling load and displacement as required for a range of testing conditions. The system is equipped with a load cell having a full-scale range of 250 N and load precision of 0.01%. When required by the magnitude of flexural load to failure, a load cell with full-scale range of 2.5 kN was used, also with a load precision of 0.01%.

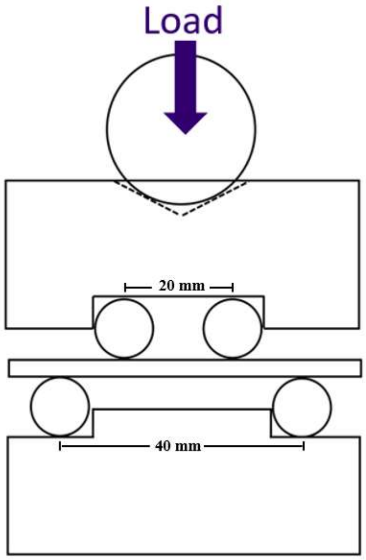

Figure 2.4: Schematic diagram of the 1/4 point 4-point bend fixtures used for flexure testing. All pieces were constructed from high purity alumina.

Ambient condition tests were conducted with the 4-point bend fixture placed on a ceramic plate on the base of the universal load frame. A sample was placed into the fixtures and aligned before being centered under a loading rod attached to the load cell. A small compressive pre-load of ~5 N was applied before the test was started. Flexural tests were completed under displacement control that corresponded to a specific magnitude of loading rate. The samples were loaded until fracture, after which the test was discontinued and the fractured sample was inspected.

In addition to testing under ambient conditions (within air and at room temperature), testing was conducted with specific environmental conditions as required by the contracting company. For the first batch of dense 38% MMA components tested, 120 samples were tested at a temperature of 850°C in an air environment containing 3.5% H_2O by volume (or moisture by volume (MBV)). Temperature was controlled by a Thermolyne 49700 series benchtop furnace placed within the Instron load frame testing environment as shown in Figure 2.5. Flexure tests were conducted within this furnace with load applied from a loading rod which passed through an opening in the top of the furnace. The fixtures were placed into the furnace with a sample introduced at or near ambient conditions. Then the temperature was raised up to the desired set point as specified by the required testing condition. It is important to note that no pre-load was applied to the samples as the environmental variables were being set. A pre-load was only applied right before the test was performed.

Figure 2.5: Image of the high temperature flexure setup placed inside the furnace. A Thermolyne 47900 series bench top furnace is placed within an Instron E1000 load frame.

Once the temperature was close to the set point, moisture was introduced to the furnace chamber via two Honeywell humidifiers. Real-time moisture measurements were obtained using a MAC125 Moisture Analyzer from MAC Instruments. The moisture level was adjusted as needed until the desired moisture set point was obtained. Once all environmental levels were set properly, they were maintained for 1 hour to allow for stabilization and equilibrium before testing was conducted. The procedure for pre-loading and testing was the same as for ambient tests.

The evaluation of the material from dense 38% MMA components was conducted in two major stages. Each stage used samples from a batch of material provided by LGFCS that had been obtained from the original manufacturer. Testing within the two stages included different environmental conditions. The first stage of evaluation consisted of testing a total of 150 samples. Of this total, 30 samples were tested under ambient conditions at a loading rate of 0.009 mm/sec. The remaining 120 samples were divided into four groups of 30 samples and were tested under the same environment of 850°C and 3.5% moisture by volume in the surrounding air. The four groups were evaluated at four different loading rates, which ranged from 0.09 mm/sec to 0.00009 mm/sec, and included 0.09, 0.009, 0.0009 and 0.00009 mm/sec. The second stage of testing consisted of 60 samples that were divided into two groups of 30 samples. All of the second stage samples were tested under conditions of 50°C and 3.5% moisture by volume in the surrounding air. One group of 30 samples was tested at a rate of 0.09 mm/sec and the other at 0.00009 mm/sec. The number of samples evaluated for each test group (30) was used to conform to ASTM C1161 where the minimum number of samples needed for estimating strength distribution parameters with reasonable confidence limits is 30. Test groups of 30 samples under each set of conditions were used consistently throughout this study.

The sample dimensions were used to calculate the moment of inertia of the samples, and the fixture dimensions and failure load were used to estimate the maximum bending moment and the corresponding stress of the MMA samples at fracture. For the dense 38% MMA sample geometry, the moment of inertia for a rectangular cross section was calculated using Equation 2 where b and h are the sample dimensions in mm.

$$I_x = \frac{bh^3}{12} \tag{2}$$

The maximum bending moment was determined based on the ¼ point 4-point bend spans as described by Equation 3 where F is the load at failure in Newtons and L is the outer roller span in mm.

$$M_{max} = \frac{1}{8} * F * L \tag{3}$$

The maximum stress at failure (MPa) was then found through Equation 4 using the moment of inertia, maximum bending moment and entering a value for c, which is the distance from the neutral axis to the tensile surface of the bend specimen.

$$\sigma_{b,max} = \frac{M_{max} * c}{I_x} \tag{4}$$

2.3 Porous MMA Tubes

The porous MMA tubes were received in the form of 250 mm long sections with 15 tubular e-channels along the full length as shown in Figure 2.6. To obtain flexural samples from the large components that conformed to the geometry specified by ASTM C1161 [32], the tubes were first sectioned into four equal-length pieces of approximately 63 mm in length. A commercial adhesive tape was used to attach the long tube components to a steel plate. The Chevalier slicer/grinder was used to perform sectioning using the same abrasive cutting wheel as described previously. Due to the porous structure of this MMA material, more aggressive sectioning conditions were used than those applied for sectioning the dense components. The coarse and fine grind down-feed intervals were increased to 0.13 mm and 0.051 mm/pass, respectively, and the feed rate was increased to approximately 90 mm per minute. All other settings were identical to those used for the dense materials in the previous section.

The individual sections cut from the previous step had the final specimen length of just over 60 mm. The next steps were used to obtain the final specimen dimensions. Each section was bonded to a glass sheet mounted on top of a steel plate following the procedures used for sectioning the dense 38% MMA components. The slicer/grinder was then used to make sections extending along the length of the tubes to obtain the final cross section as shown in Figure 2.6. Each sample was cut so that the cross section included two complete tube channels, two vertical channel walls, and two half-channels (one on each side). Following this approach, four tube specimens were obtained from each individual section and a total of 16 samples were taken from each full tube component that was received. After completion of the sectioning process, all samples underwent the drying process outlined previously. A chamfer was introduced along the edges in the same manner as outlined previously to remove any burs from sectioning. That was applied as a finishing process to improve the edge geometry for measurement of dimensions and also to reduce the chance for failure to initiate from edge chips emanating from the bur.

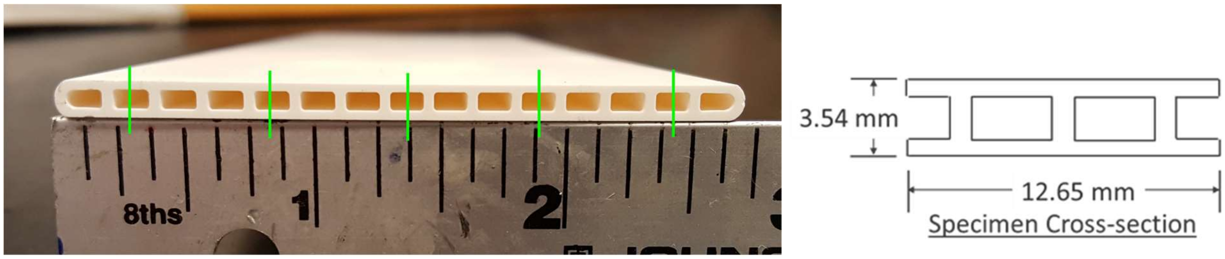

Figure 2.6: Details of the porous tube specimens used for flexure testing and determination of the strength distributions. Left - A tube component cross-section with vertical marks to indicate its division into four samples. Right - Final sample cross-section geometry with a length of approximately 63 mm.

Flexural testing of the porous MMA samples was performed in air at ambient and elevated temperatures (850°C) in an identical fashion to the dense 38% MMA materials. Testing conditions required 50% moisture by volume, which was a factor of magnitude greater than that used in testing of the dense components and constituted a moisture level that exceeded the capacity of the previously used humidifiers. To achieve this higher moisture content in the testing chamber of the furnace, a water bottle with a needle valve was implemented to control the flow of water according to a dripper arrangement. The dripping rate was adjusted to achieve the desired moisture content at the temperature of the furnace using the commercial moisture analyzer. In addition to the unique moisture content, a specific gas composition was introduced into the furnace for testing the tube material, which consisted of 47.5% nitrogen and 2.5% hydrogen. To achieve the specific nitrogen and hydrogen content at the desired levels, a pre-mixed gas of 95% nitrogen and 5% hydrogen was fed into the furnace chamber from a compressed gas cylinder. The gas was introduced into the furnace once the desired moisture content was reached and remained flowing until the end of the flexural test. For tests involving high moisture levels and gas, the furnace chamber was sealed to better maintain environmental conditions and limit the extent of gas needed to achieve the desired levels. Specifically, a high temperature bagging material was used to encapsulate the furnace and a spongey tape was used for sealing in locations where the chamber was subject to leaking. The evaluation of the porous MMA tube material involved a total of 120 samples; 30 samples were tested under ambient conditions at a loading rate of 0.009 mm/sec. Another 30 samples were tested at a temperature of 850°C in air at the same loading rate. The remaining 60 samples were split into two groups and tested at rates of 0.09 mm/sec and 0.0009 mm/sec, while exposed to an environment consisting of 50% moisture by volume in the surrounding air, 47.5% nitrogen and 2.5% hydrogen. Note that the tube samples subjected to the lowest loading rate were tested at 0.0009 mm/sec and not 0.00009 mm/sec due to the required deadline stipulated by LGFCS for the completion of testing. The slower rate would have added a substantially larger period of time to the testing protocol. There was no limitation to the testing results posed by this choice.

After fracture of the specimens, the strength associated with failure was estimated following the approach used for the dense MMA. The same equations were used to obtain values for the maximum bending moment and stress at failure. The moment of inertia was calculated using the subtraction method to account for the tube geometry and its deviation from a basic rectangular cross section.

2.4 Dense MMA Manifolds

Dense manifolds of 38% MMA composition were received as 18-inch-long components as shown schematically in Figure 2.7; these were referred to as the M3 manifolds. The manifold component had four large tube channels passing along the full length with three vertical sections. In addition, one surface of the manifolds contained a series of machined slots that repeated along the entire length. Specimens were sectioned from one surface of the manifold components (referred here as the bottom surface) to enable flexure testing as seen in Figure 2.7.

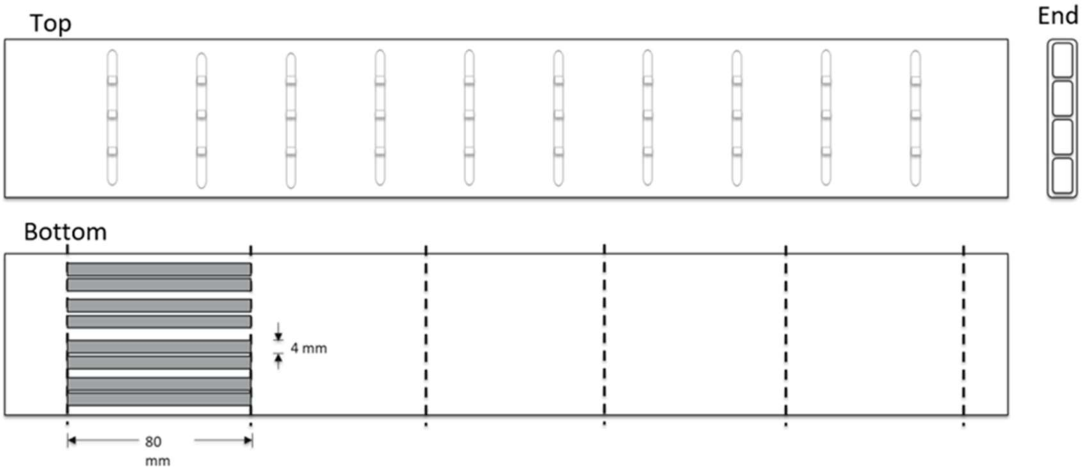

Figure 2.7: Diagram of a 38% MMA manifold component (LG designation M3) with section lines to indicate where samples were obtained. The bottom view shows where eight specimens were obtained from the abrasive slicing process.

To obtain consistent test specimens, the manifold was cut into five equal-length sections as shown in the bottom view of Figure 2.7, which provided specimen lengths of 80 mm. As with the porous MMA tubes, the manifolds were attached to a steel plate with a commercial adhesive tape. Abrasive slicing was performed with the Chevalier slicer/grinder using a coarse down-feed interval of 0.25 mm and an x-axis feed rate of approximately 50 mm/min.

Each of the five primary sections of the manifolds were then attached to the steel plate with adhesive so that the surface with the machined slots (top surface in Figure 2.7) was facing down. The slicer/grinder was then used to introduce longitudinal sections passing through the bottom surface of the manifold as shown in Figure 2.7. Each tube channel (between two vertical sections) had enough space so that two 4 mm wide beams could be obtained. In this manner, each of the five primary manifold sections provided eight specimens for a total of 40 per manifold component. Each of the specimens had average width, thickness and length of 4, 1.7 and 80 mm, respectively. It is important to comment that the slicing operations were performed in a different manner from those described for the previous dense and porous components. Here, the sectioning was performed in one pass with a feed rate of approximately 2.5 mm/min. The blade was positioned so that no cutting took place on the slotted side of the manifold. This method was found from preliminary testing to provide the best level of orthogonality in the final samples and eliminated the chance of burs or chipping to develop when the sample separated from the rest of the manifold. Because the samples were not supported by a glass foundation as in the previous sectioning, this approach was necessary to achieve the same edge quality.

The surface facing the outside of the manifold component was consistently used as the surface of the specimens exposed to tensile stress during flexural testing. Due to manifold component inconsistency, particularly the internal geometry of the manifold tubes, several samples did not have a constant thickness perpendicular to the sample length. To remedy this problem, the sample surface opposite the surface to be exposed to tension was polished to achieve orthogonality with the other sides of the sample. Since that surface was subjected to compression, and sample failure initiated from the tensile surface, no limitation was presented by this process.

A total of 60 manifold samples were tested in this study, which were prepared from two large M3 manifolds (nomenclature of supplier). All samples were subjected to environmental conditions of 50°C and 3.5% moisture by volume in the surrounding air. Two loading rates were utilized in displacement control, including 0.09 and 0.00009 mm/sec. The 30 tests conducted at each rate consisted of 15 samples that were obtained from each of the two different manifold components to minimize the chance of bias caused by the manifold history or differences in processing and handling. After failure, the strength of each specimen was calculated using an identical procedure as that used for the dense 38% MMA specimens according to Section 2.2.

2.5 Porous YSZ Tape

A porous yttria-stabilized zirconia (YSZ) tape material was also received from LGFCS in Canton, OH without additional information regarding its chemical composition or details of processing. The material was received in the form of rectangular strips with lengths of approximately 50 mm. The samples had a uniform thickness of approximately 0.80 mm, but there was variation in the sample width that ranged between 3 and 3.5 mm. Furthermore, due to the materials being cut into strips prior to sintering, many of them were warped and the specimen edges were rough and inconsistent. A special fixture and 800 grit silicon carbide abrasive paper was used to polish the sample edges until they were straight and smooth on both sides. The sides were also made to be as orthogonal as possible with respect to the top and bottom surfaces of the samples. As with previous materials, a small chamfer was introduced along the long edges of each sample. All tape samples underwent an identical drying process as the previously tested dense and porous MMA materials before evaluating the mechanical behavior.

The YSZ samples were subjected to 4-point flexure testing to failure using the same fixture geometry with ¼ point arrangement. Due to their thin cross sections, extra care was taken during arrangement of the porous tape materials in the fixtures and their alignment. Due to the small thickness, the failure loads were extremely small, which required a reduction of the pre-loads to ~0.2 N, when applied. It is important to note that the weight of the upper fixture and rollers was a significant percentage of the overall load. A total of 60 tape samples were tested, including 30 samples for each loading rate of 0.09 mm/sec and 0.00009 mm/sec. All samples were exposed to an environment of 850°C, 50% moisture by volume in a gas environment of 50% air, 47.5% nitrogen, and 2.5% hydrogen. The procedures used for achieving environmental conditions were consistent with those used for the previous porous MMA tube materials tested. Furthermore, the strength of the samples was calculated in an identical manner to the methods used for evaluating the dense 38% MMA samples.

2.6 Fracture Toughness of Dense MMA (38% Alumina Content)

The second batch of dense 38% MMA components that were described in Section 2.2 were also used in evaluating the facture toughness of this material. Following sectioning of specimens from the thin portion of the dense MMA components (Figure 2.3), the remaining materials were sent to International Ceramic Engineering to be ground to obtain specimens for evaluating the fracture toughness. The thick sections of the dense MMA components were ground on three sides to obtain a sample cross-section geometry of 3 mm x 4 mm; the specimens had a length of approximately 70 mm. One of the 4 mm sides remained unground to preserve the as-manufactured surface condition of the material. A total of 20 samples were prepared for performing the fracture toughness evaluations, which were divided into four separate groups.

The procedure for conducting fracture toughness evaluations followed those defined by ASTM C1421 [46] for the surface crack in flexure method. Surface pre-cracks were introduced with a diamond Knoop micro-indenter at an indentation load of 30 N (~3 kg) using the Instron universal testing system. The indentations were introduced with the long diagonal of the indent oriented perpendicular to the length of the sample. Of the 20 samples tested, 10 were indented on the unground surface of the dense sample after a very light polish. The polish was performed to obtain a surface free of major topographical deviations that could interfere with the surface cracks. The remaining 10 samples were polished down approximately 250 μm from the unground surface using 320 grit abrasive paper followed by 800 grit abrasive paper. An indentation was applied on the polished surface, also centered with respect to sample length and width. For each set of 10 samples, half were tested at 50°C and the other half at 850°C. All samples were tested under exposure to 3.5% moisture by volume in a surrounding standard air environment.

Flexure testing of the samples was conducted using a 3-point arrangement with outer span of 40 mm according to ASTM C1421 [46]. The indented surface of the samples was oriented to achieve tensile stress. The flexural tests were conducted until sample failure under displacement control at a loading rate of 0.05 mm/sec following the procedures outlined for previous materials. Estimating the fracture toughness required calculation of the stress at failure, in addition to the stress intensity factor for the penny-shaped pre-crack introduced by the indentation of the beam. The pre-crack size was measured for each sample using scanning electron microscopy. A diagram of the sample geometry with labels and dimensions is shown in Figure 2.8.

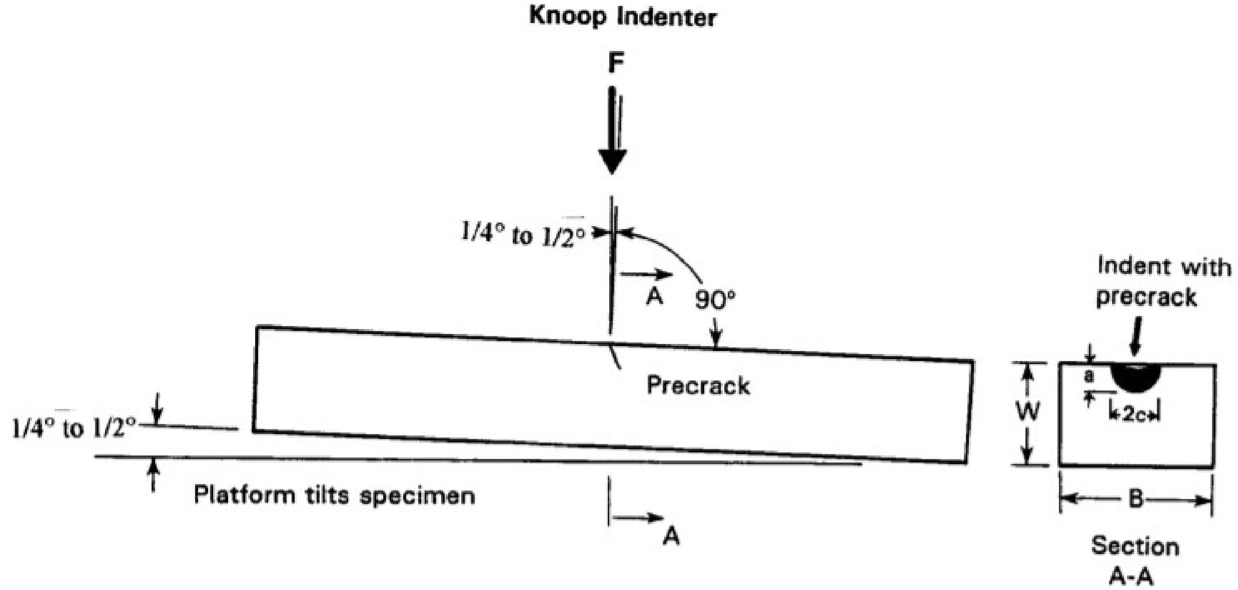

Figure 2.8: Schematic diagram of the indentation procedure and resulting pre-crack geometry for a fracture toughness evaluation. Image taken from *[46]*.

The expression for fracture toughness is given by Equation 5 where Y is the stress intensity factor coefficient, P_{max} is the maximum load in Newtons, S_0 is the outer span in mm, S_i is the inner span in mm, B and W are the sample dimensions, and a is the pre-crack depth.

$$K_{Isc} = Y\left[\frac{3P_{max}[S_0 - S_i]10^{-6}}{2BW^2}\right]\sqrt{a} \tag{5}$$

Depending on the size and shape of the measured pre-crack, the stress intensity factor coefficient can be highest at either the surface or at the deepest part of the pre-crack. In the deep case, Y can be calculated via Equation 6.

$$Y_d = \frac{[\sqrt{\pi}MH_2]}{\sqrt{Q}} \tag{6}$$

where Q, M, and H_2 are calculated according to

$$Q = 1 + 1.464[a/c]^{1.65} \tag{7}$$

$$M = \left[1.13 - 0.09[a/c]\right] + \left[-0.54 + \frac{0.89}{\left[0.2 + [a/c]\right]}\right][a/W]^2 + \left[0.5 - \frac{1}{\left[0.65 + [a/c]\right]} + 14[1 - a/c]^{24}\right][a/W]^4 \tag{8}$$

$$H_2 = 1 - \left[1.22 + 0.12[a/c]\right][a/W] + [0.55 - 1.05[a/c]^{0.75} + 0.47[a/c]^{1.5}][a/W]^2 \tag{9}$$

For the case where Y is highest at the surface, it can be calculated according to Equation 10.

$$Y_s = \frac{\left[\sqrt{\pi} M H_1 S\right]}{\sqrt{Q}} \tag{10}$$

where H_1 and S are defined as

$$H_1 = 1 - \left[0.34 + 0.11[a/c]\right][a/W] \tag{11}$$

$$S = [1.1 + 0.35[a/W]^2]\sqrt{a/c} \tag{12}$$

2.7 Strength Distributions

Based on the importance of flaws to the strength of ceramics, it is important to characterize the strengths using a stochastic model rather than a deterministic definition. One of the most common approaches for describing the strength distributions of ceramic components is using the Weibull weakest link model [47]. Therefore, the strengths of each fuel cell component and conditions of analysis were evaluated using a Weibull model. For this purpose, the strength distributions were ordered in terms of the stress at failure from lowest to highest. Each measure of strength is assigned a rank with the lowest stress being rank 1 all the way to the highest with largest strength. For each stress at failure, an estimate of the proportion of the population that will fail from that stress level must be established. This was completed using the median ranks method where the median ranks were assigned through the following formula [33, 48]

$$Median\ Rank = \frac{Stress\ Rank - 0.3}{Number\ of\ Samples - 0.4} \tag{13}$$

where the number of samples is the total number of samples tested in the group to be described. The median rank is then treated to describe the probability of failure at each stress level by Equation 14.

$$P_f = ln(ln\left(\frac{1}{1 - Median\ Rank}\right)) \tag{14}$$

This probability of failure is then plotted in terms of the natural log of the stress at failure to obtain the Weibull strength distribution. The data can then be fit with a linear regression trendline to obtain the Weibull parameters. The trend line follows the standard y = mx + b format where m is the Weibull modulus and the modulus of rupture (MoR) is equal to

$$MoR = e^{b/m} \tag{15}$$

2.8 Slow Crack Growth Responses

SCG models are used to quantify the extent of rate dependence in the strength of a material according to

$$\sigma_f = D\dot{\sigma}^{1/_{1+n}} \tag{16}$$

where D and n are the slow crack growth coefficient and exponent, respectively.

Following the procedures outlined in ASTM C1368 [44], this method requires calculation of the stress rate in MPa/sec for each individual sample evaluated in flexure and plotting the strength in terms of the stress rate. Since tests were conducted in displacement control with a specified rate, the first step is to find the loading rate in N/s for each sample based on the load versus displacement data. For the materials tested, the load increased linearly with displacement due to the linear elastic behavior of the ceramic samples, regardless of temperature. Note that the load at failure in this case refers to the final load applied by the load frame and does not consider the applied load from the upper fixtures since it is constant. Therefore, the loading rate was determined as the slope of the load versus displacement curve according to

$$Loading\ Rate = \dot{P} = \frac{Load\ at\ Failure - Initial\ Preload}{Time\ at\ Failure - Initial\ Time} \tag{17}$$

The loading rate is then used to find the stress rate through Equation 18 where L is the outer span in mm and b and d are specimen dimensions in mm.

$$Stress\ Rate = \dot{\sigma} = \frac{3\dot{P}L}{4bd^2} \tag{18}$$

Once the stress rates were found for all of the samples evaluated for a specific group, the log of stress rate is plotted against the log of failure stress for all the sample pairs in the group. A linear regression is then applied to this data, which takes the form

$$\sigma_f = \frac{1}{1+n} log\ \dot{\sigma} + log\ D \tag{19}$$

where σ_f is the failure stress including fixture weight, D is the SCG coefficient and n is the SCG exponent.

Chapter 3 - Results

3.1 Dense 38% MMA Strength Distributions

To characterize the strength distribution of the dense MMA endcap components, Weibull plots were constructed using the flexure strength. Results for the dense MMA evaluated under ambient conditions (air and room temperature) and subjected to a loading rate of 0.009 mm/s are shown in Figure 3.1; the data presents the probability of failure in terms of the natural log of the strength. The data exhibits a linear distribution, as evident from the consistency with a linear trendline. Using a best-fit to the data resulted in a Weibull modulus of 20.7 and a modulus of rupture (MoR) of 302.2 MPa.

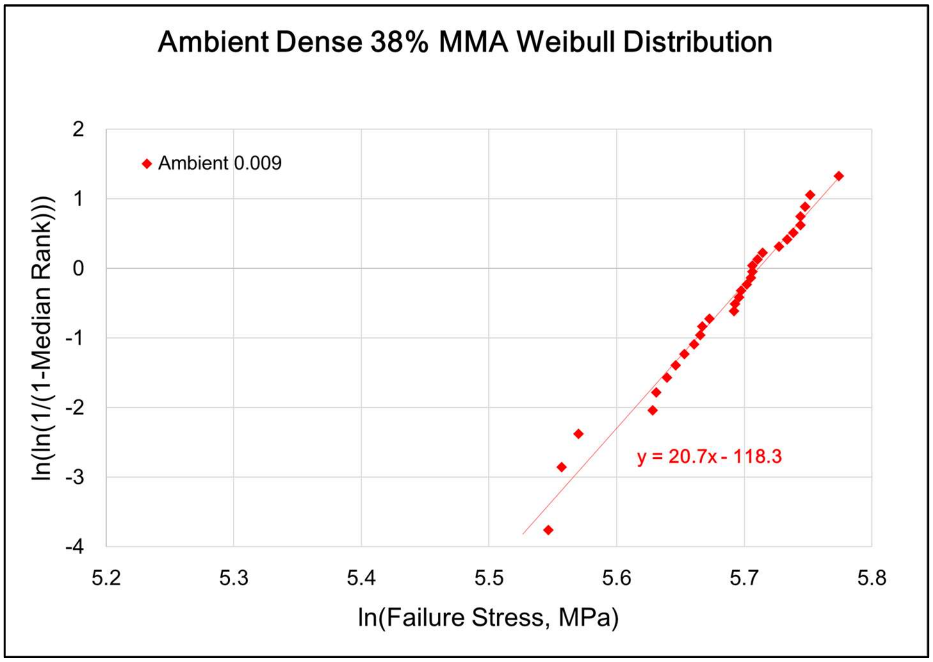

Figure 3.1: Weibull response for the first batch of dense 38% MMA specimens evaluated under ambient conditions and loading rate of 0.009 mm/s.

Results from testing within the ambient conditions were then compared to strength distributions for the sample groups tested at 850°C and 3.5% moisture by volume, including rates from 0.00009 to 0.09 mm/s. A comparison of these five strength distributions for the 38% dense MMA end caps is presented in terms of a Weibull plot in Figure 3.2. As evident from the relative positions of the data, the increase in temperature and moisture promoted a decrease in strength. It was found that the MoR for all four sample groups tested under high temperature and moisture conditions were lower than for the group tested at ambient conditions (Table 3.1). Although the Weibull modulus was similar for the strength distributions obtained from evaluations at room and elevated temperature, the group subjected to the fastest rate of loading appeared to exhibit a small reduction in the Weibull modulus. The lower Weibull modulus suggests that the conditions caused lower consistency in the weakest links contributing to failure.

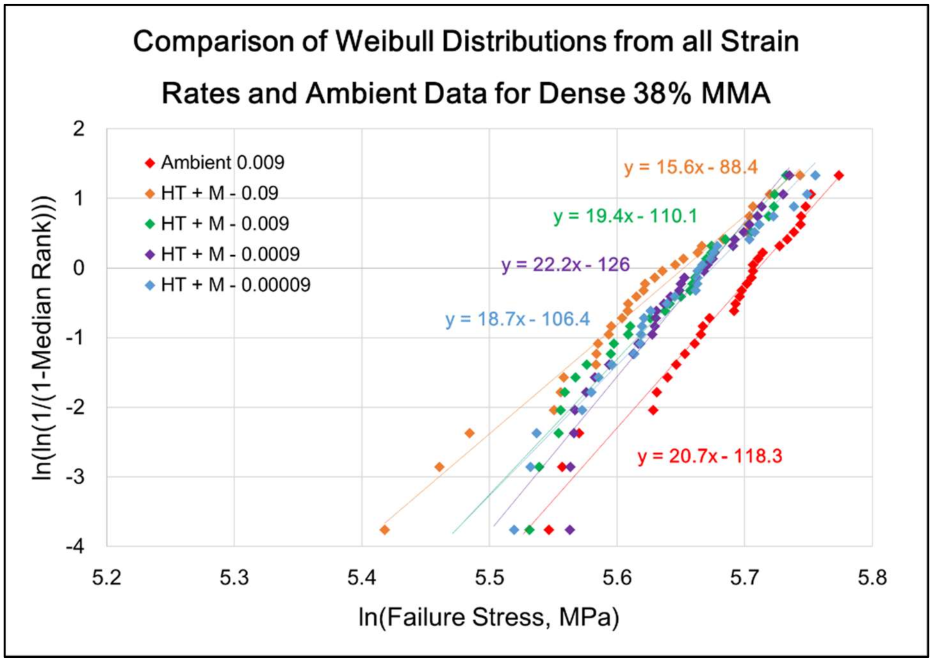

Figure 3.2: A comparison of the Weibull strength distributions for the first batch of dense 38% MMA specimens under all conditions considered. HT + M - # indicates high temperature (850°C) and moisture (3.5% by volume), followed by the displacement rate (mm/s).

The Weibull parameters (m and MoR) obtained from results of the flexure strength distributions for all of the dense 38% MMA samples are listed in Table 3.1.

Table 3.1: Summary of Weibull parameters for all test groups for the first batch of dense 38% MMA.

Room Temp, Air		
Rate (mm/sec)	**m**	**MoR (MPa)**
0.009	20.7	302.2
High Temp, 3.5% MBV		
Rate (mm/sec)	**m**	**MoR (MPa)**
0.00009	18.7	291.4
0.0009	22.2	290.0
0.009	19.4	289.3
0.09	15.6	284.9

To examine the dependence of strength on the rate of loading, the average strength of the dense MMA tested at 850°C was plotted in terms of loading rate in Figure 3.3. As evident from this presentation there is no statistical difference in the average strength between the four groups of dense MMA samples tested at high temperature and with 3.5% MBV.

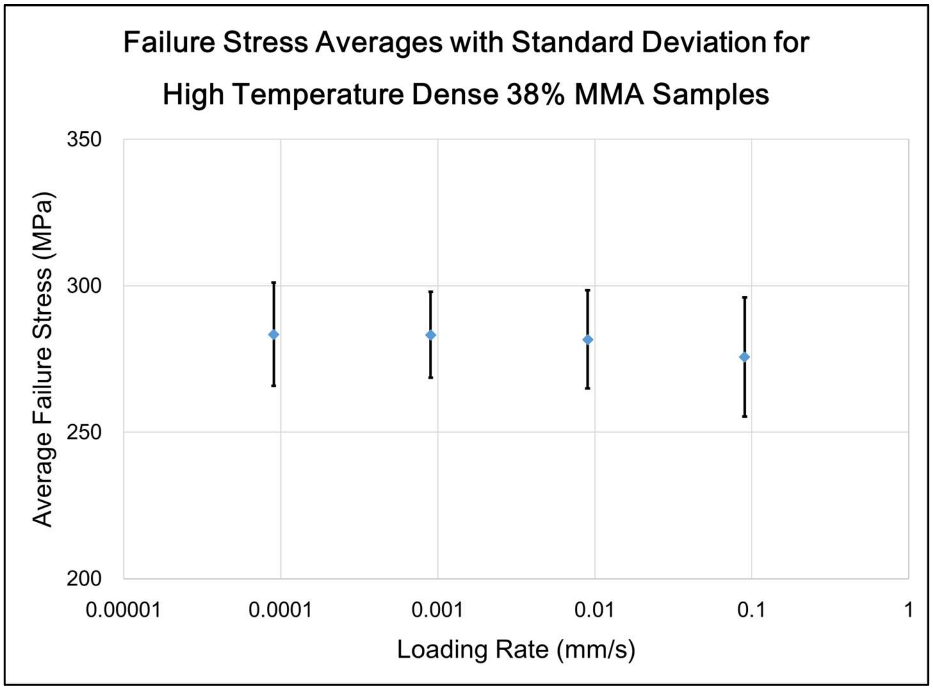

Figure 3.3: A comparison of average failure stresses of the dense 38% MMA end caps evaluated at 850°C and with 3.5% moisture by volume. The data at each rate is described in terms of the average strength and one standard deviation.

To assess the rate dependence in the strength distributions at high temperature, the average strengths were plotted in terms of the stress rate as shown in Figure 3.4. Using the power law model defined by equation 16, the SCG response was characterized in terms of the model parameters. The result of this analysis can be seen in Figure 3.5. Based on a best fit assessment of the experimental data, the SCG coefficient D = 281 MPa and the exponent n = -251.

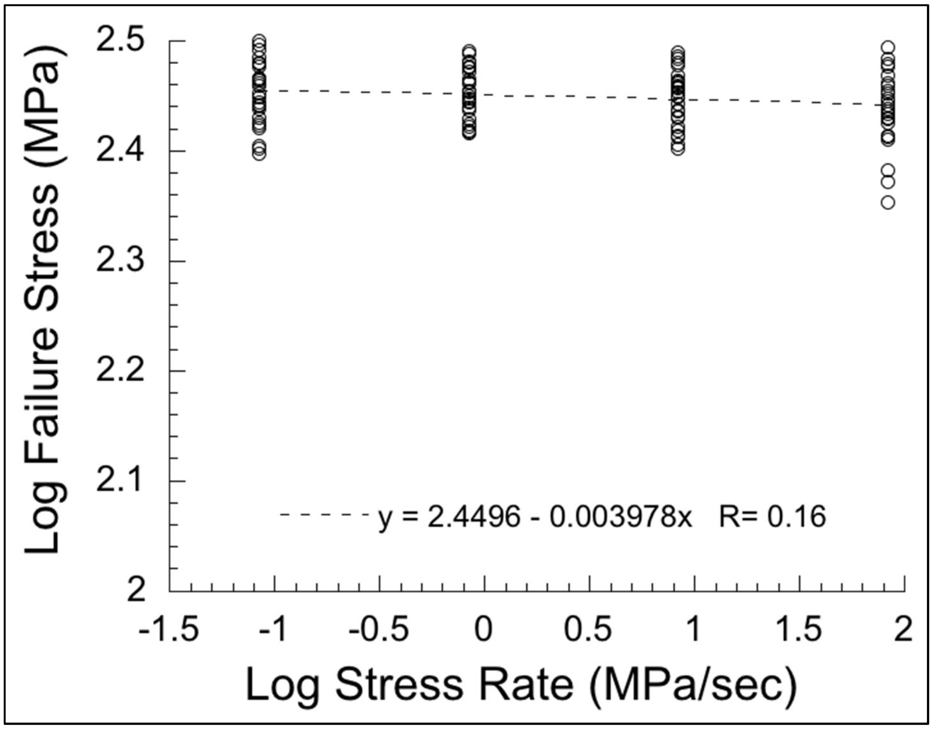

Figure 3.4: Slow crack growth assessment for the first batch of dense 38% MMA tested at 850°C and 3.5% moisture by volume. The SCG coefficient and exponent obtained from this analysis are 281 MPa and -251 respectively.

In addition to flexure testing, a microscopic analysis was performed on the dense components to identify characteristics that could contribute to the strength. An initial exploration of the surface of the dense components was completed via optical microscopy at low magnifications. This evaluation revealed the presence of surface pores, and an example is presented in Figure 3.5 in an area of the component where a large group of pores were identified.

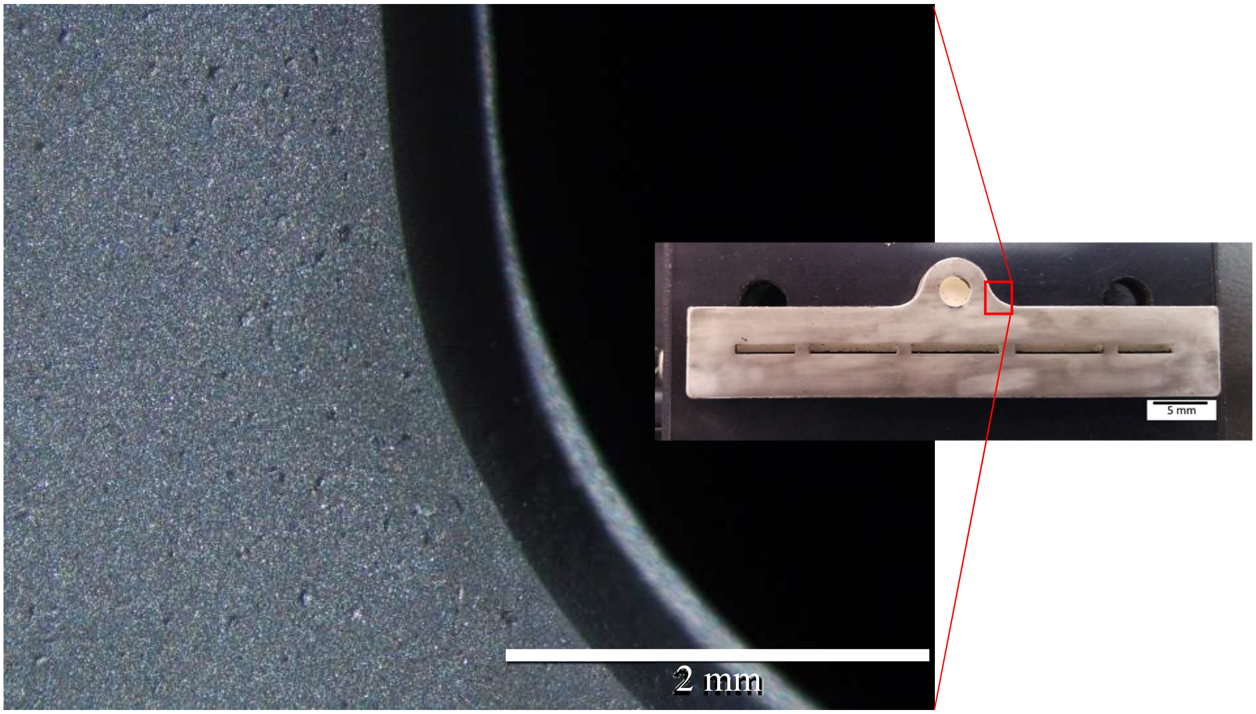

Figure 3.5: An example of pores scattered across the surface of a dense 38% MMA component located near an area of curvature.

The strength of one of the dense MMA samples tested at 850°C and 3.5% moisture by volume at a rate of 0.00009 mm/s was 143.4 MPa, a value nearly 50% lower than the average of 283.4 MPa of that group. A fractographic analysis of the tensile surface of that specimen with a stereomicroscope revealed that a large surface pore served as the origin of failure and the low strength (Figure 3.6); the flaw had an effective diameter of 550-600 µm. Although flaws of this size were uncommon, smaller surface pores were also present and served as the origins of failure of other samples. Nearly all samples that achieved the lowest strengths of the individual groups exhibited dominant surface pores that were identified as the origin of fracture.

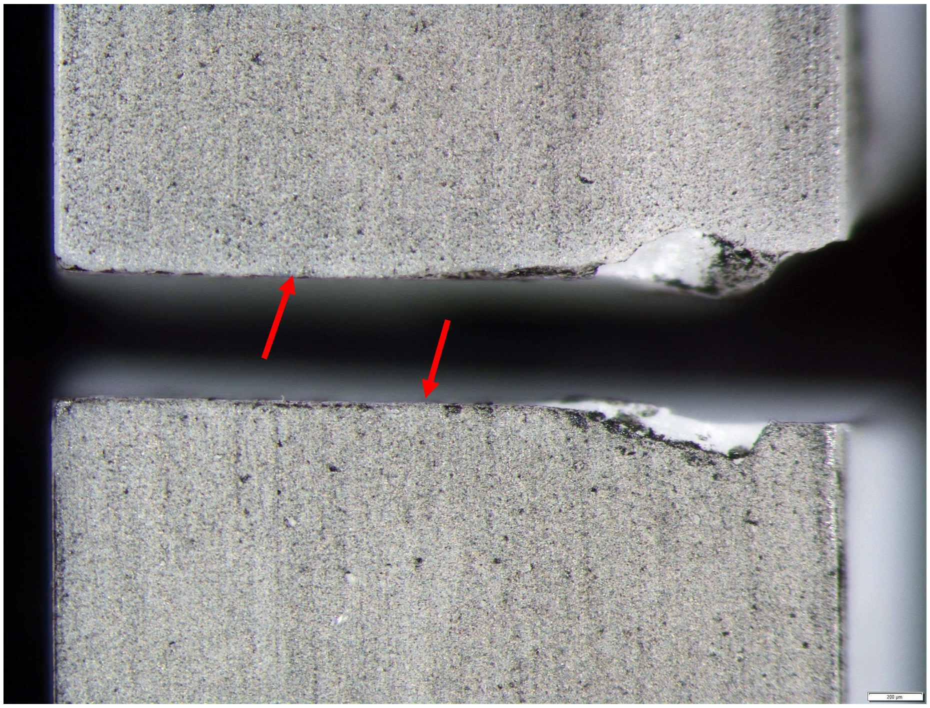

Figure 3.6: Two halves of a fractured dense 38% MMA sample from the first batch with a pore at the location of fracture. The flat surface in the plane of the page is the surface exposed to tensile stresses under bending. The fracture surface is perpendicular to the plane of the page and is indicated with red arrows. The scale bar at the bottom right represents 200 μm.

In addition to the evaluation of surface pores, an evaluation of interior porosity was performed through scanning electron microscopy (SEM). A representative specimen of the dense 38% MMA was broken in two pieces to enable visualization of the microstructure of the internal cross-section. Sputter coating was used to prevent sample charging and provide ample electron conductivity. It was found that pores of varying size were distributed throughout the cross-section as shown in the SEM image in Figure 3.7. A range of pore sizes (from 3 to 60 μm) and shapes can be seen. The pores could be separated into three major classes as follows: Class 1 pores were smaller than 5 μm effective diameter, which is consistent with the size of grains in the material, Class 2 pores were 10-20 μm in diameter, and Class 3 pores were very large with a size exceeding 40 μm. The largest pores were not circular, but rather existed as compressed discs, apparently a result of the powder consolidation that occurred during the action of pressing.

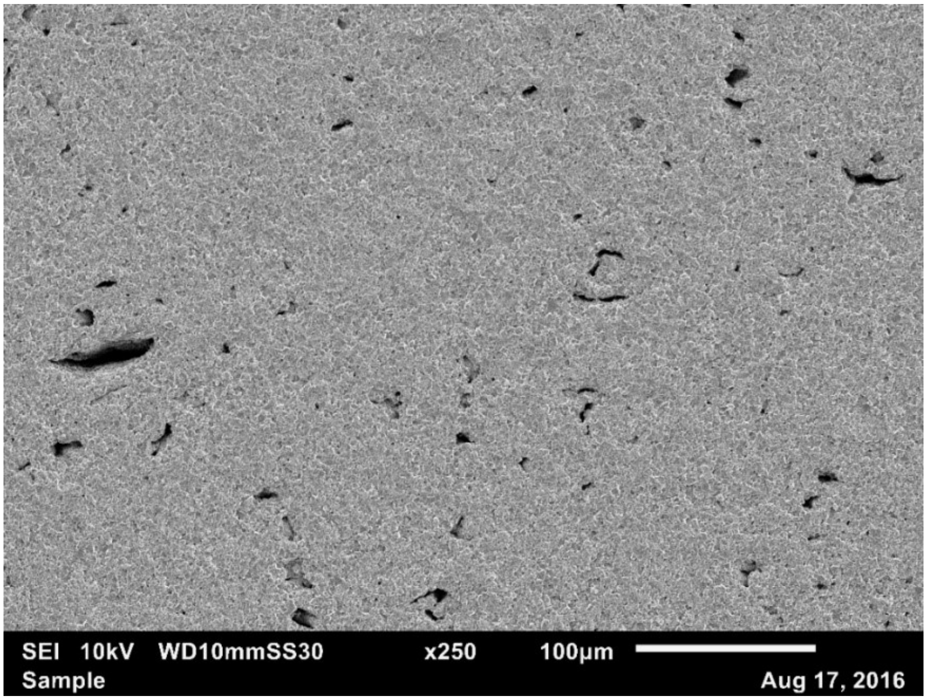

Figure 3.7: SEM micrograph of internal porosity in a sample of dense 38% MMA from the first batch.

3.2 38% Dense MMA Strength Distributions – Second Batch

After completing an evaluation of the dense 38% MMA at ambient conditions and 850°C, a second batch of samples from the same manufacturer were tested in 4-point flexure to failure, but at 50°C and 3.5% MBV. This condition was chosen according to concern that slow crack growth was occurring in the dense MMA components at relatively low temperatures. The strength distributions for the second batch of material are shown in terms of a Weibull plot in Figure 3.8. As evident from the results in this figure, the responses were different from those obtained at room temperature or 850°C as shown in Figure 3.2.

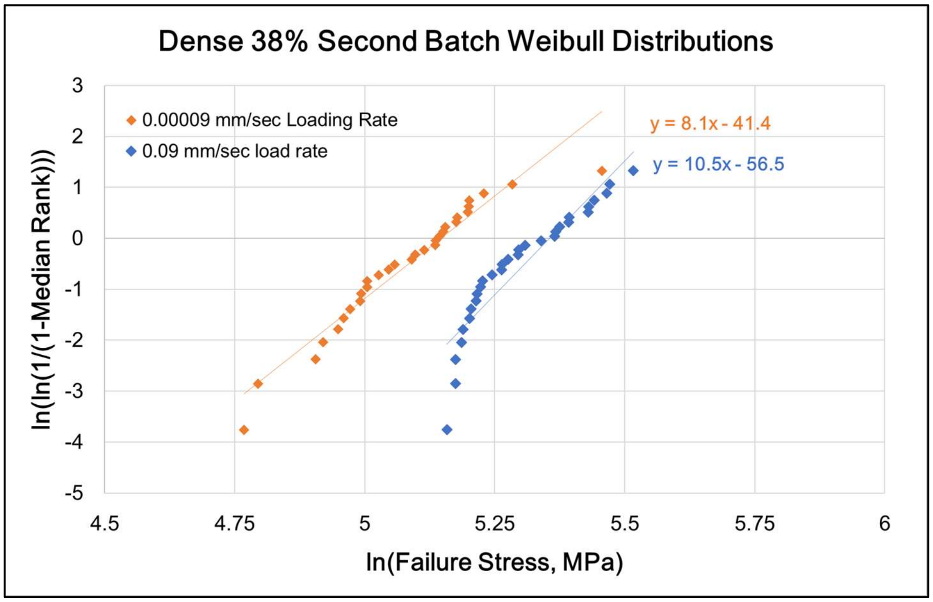

Figure 3.8: Weibull responses for the second batch of dense 38% MMA. The samples were evaluated at 50°C and 3.5% moisture by volume. Note the bimodal strength distribution, particularly for the samples tested at the higher loading rate.

The first major difference in the results is that there was a substantial reduction in the modulus of rupture with respect to the previous evaluations. A summary of the Weibull parameters for the two different loading rates is presented in Table 3.2. The MoR obtained from results at 50°C was approximately 25 to 39% lower than that from the first batch tested at both ambient and high temperature conditions, depending on the test rate.

Table 3.2: Summary of Weibull parameters for both testing rates for the second batch of dense 38% MMA.

50°C, 3.5% MBV		
Rate (mm/sec)	**m**	**MoR (MPa)**
0.00009	8.1	171.9
0.09	10.5	211.9

Another obvious difference in the strength distributions obtained for the 50°C condition is a lower Weibull modulus at both rates when compared to the previous results. The moduli for the second batch are more than 50% lower than the first. Furthermore, it was found that the failure responses at each rate were not uni-modal (i.e. did not follow a single trend line) and could be better described if they were broken into two sub-groups as shown in Figure 3.9. This is often described as a bi-modal strength distribution due to the two distinct trends for each group of specimens.

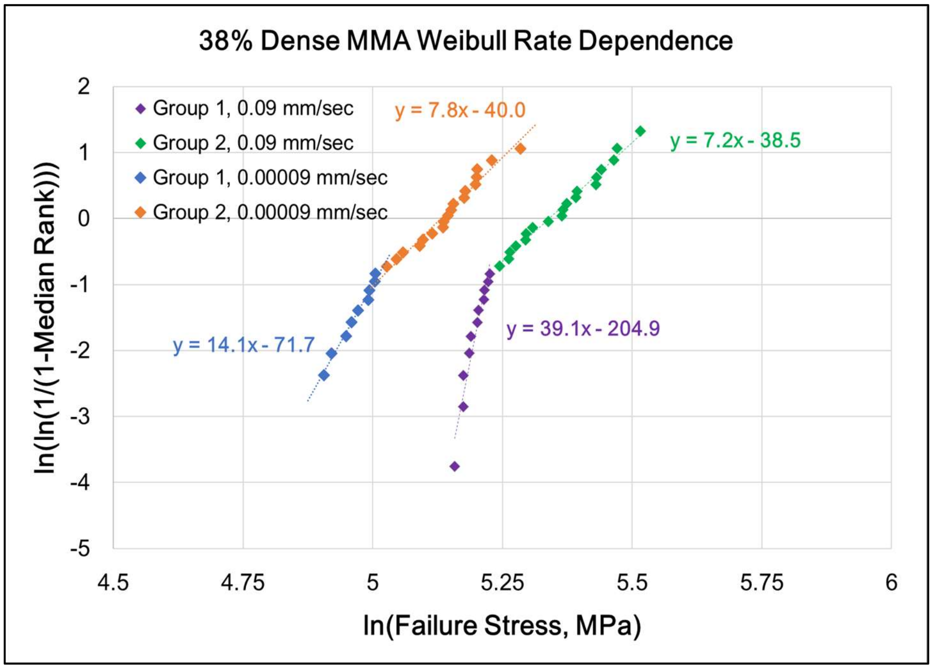

Figure 3.9: Weibull strength distributions for the second batch of dense 38% MMA samples using a bimodal treatment of the strength data. Group 1 and Group 2 at each loading rate refers to the lower and higher sample strengths of the thirty samples at each loading rate.

By dividing the responses into two groups according to the segmentation in the strength distributions, it was possible to quantitatively describe the groups with two distinct Weibull models. The Weibull distributions for the data obtained with the two different rates of loading are shown in Figure 3.9. For convenience, the strength responses obtained for flexural loading at each rate were divided into Group 1 and Group 2, which corresponded to the portion with lowest and highest relative strength, respectively. Following this approach, it was revealed that the groups of specimens with lower failure stress had a significantly higher Weibull modulus than those groups with higher failure stresses as evident in this figure. Furthermore, the samples tested at the slower rate of 0.00009 mm/s showed a reduction in MoR of approximately 40 MPa with respect to the faster rate. Consistent with the analysis of results for the previous batch of material, the SCG response was evaluated to provide a better idea of the impact of the loading rate and the results are presented in Figure 3.10.

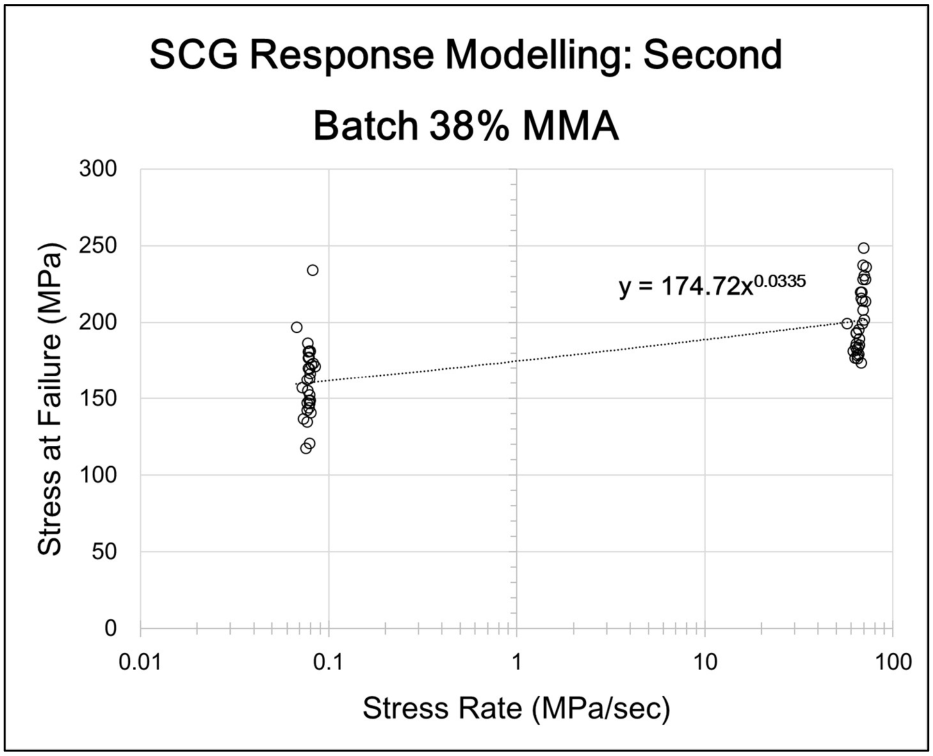

Figure 3.10: SCG model for the second batch of dense 38% MMA evaluated at 50°C and 3.5% moisture by volume in air. The SCG coefficient and exponent obtained from this analysis are 174.7 MPa and 29 respectively.

The SCG parameters were estimated from this response according to Equation 16 and resulted in a slow crack growth coefficient of 174.7 MPa and exponent of 29. The exponent indicates that the 50°C condition resulted in moderate SCG sensitivity.

To gain insight into why the strength distributions were very different between the two batches, a visual analysis of the material was conducted. It was quickly determined that the quality of the second batch of material was different from the first. An example of the material surface can be seen in Figure 3.11 where some large surface pores are documented.

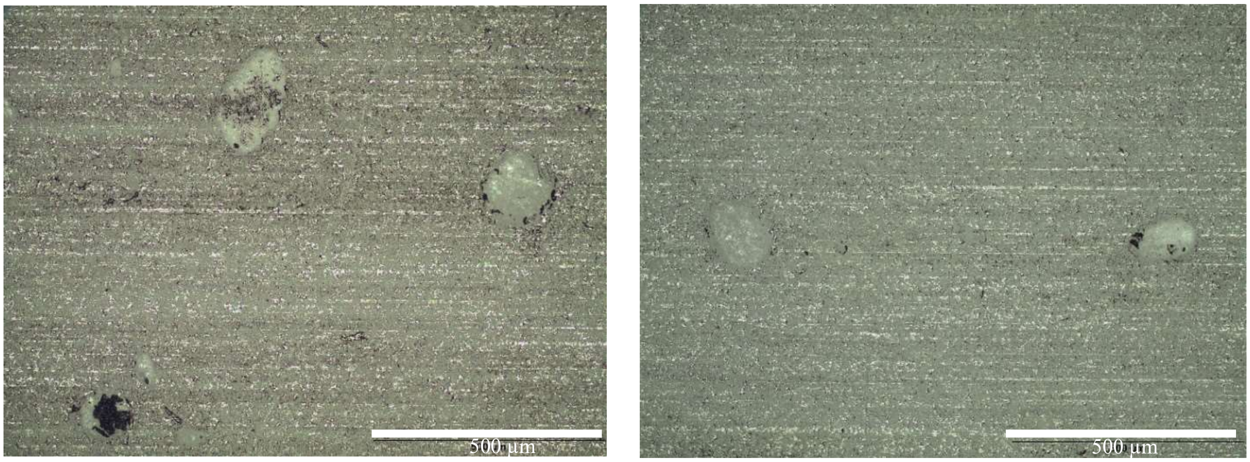

Figure 3.11: Examples of surface porosity found on the tensile surface of second batch dense 38% MMA samples.

Pores on the surface of samples from the second batch were found to be substantially larger than those found on the surface of samples from the first. Whereas the largest pores in the batch one material were around 150 µm and scarce, the largest pores in batch two ranged from 100-250 µm and were frequently found on the surfaces examined.

3.3 Porous Tube Testing

The first step in examining the mechanical behavior of the porous MMA tubes was to evaluate the influence of temperature on the strength. Figure 3.12 shows results obtained from flexure testing of samples at six different temperature levels, including the standard operating temperature for the tubes (850°C). It was found that the strength of the MMA tubes does not change significantly until reaching approximately 650-700°C. For temperatures beyond this level, the strength increases and reaches a plateau at just over 800°C with a strength nearly 40% greater than that at room temperature. Clearly the increase in strength would provide an increase in safety of the cells under the operating conditions.

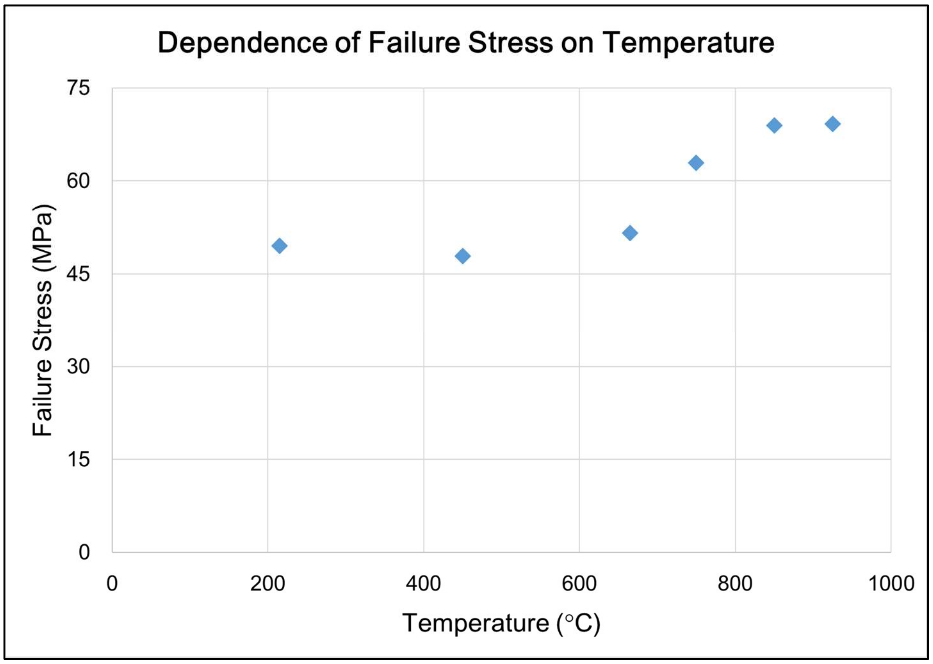

Figure 3.12: Relationship between temperature and average strength for the porous MMA tubes. These tests were conducted in air without addition of moisture.

The next step of the evaluation involved flexure testing of the tube specimens using the same framework as that used for the dense MMA components. The first condition involved testing at room temperature. The strength distribution for tube samples tested at room temperature and in an air environment is shown in Figure 3.13, as well as the Weibull model. In general, the data exhibited a linear distribution with a Weibull modulus of 31.7 and MoR of 51.1 MPa.

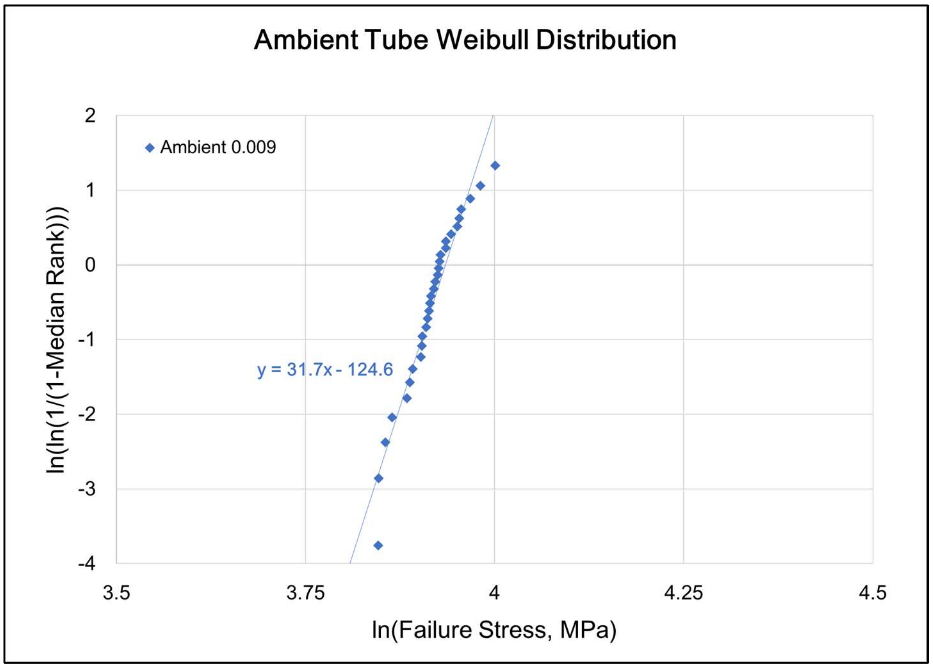

Figure 3.13: Weibull distribution for the set of porous MMA tube samples tested under ambient conditions.

Following this first step of the evaluation, the strength distributions and Weibull models were obtained for the three remaining testing conditions used for evaluating the tube specimens, including testing at 850°C at a loading rate of 0.009 mm/sec, and testing two groups at high and low stress rates at 850°C with 50% moisture and mixture of 50% air, 47.5% N_2 and 2.5% H_2. All four Weibull distributions for the porous tube material can be seen in Figure 3.14.

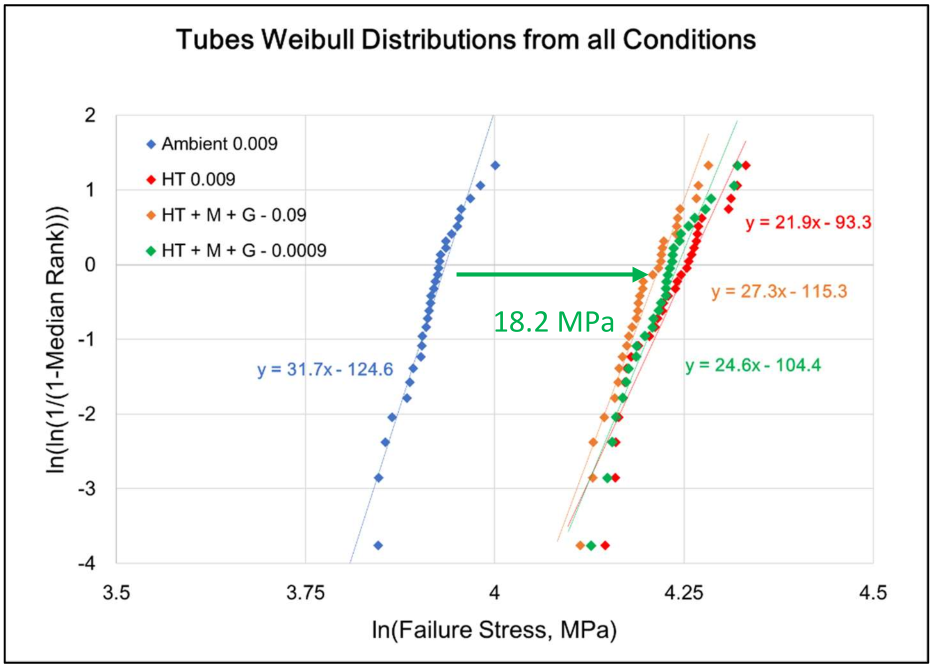

Figure 3.14: Weibull strength distributions for all porous tube samples. HT + M + G - # indicates high temperature (850°C) and moisture (50% by volume) and gas (50% air, 47.5% N_2 and 2.5% H_2), followed by the displacement rate (mm/s).

As evident from the results in Figure 3.14, the three groups evaluated under high temperature conditions showed an increase in the MoR of nearly 20 MPa with respect to the results at room temperature, an increase of over 35%. In addition, the increase in temperature caused a reduction in Weibull modulus with respect to the baseline at ambient conditions. A summary of the Weibull parameters obtained for the four groups is presented in Table 3.3.

Table 3.3: Summary of Weibull parameters obtained from the strength distributions of results for flexure testing of the porous MMA tubes. HT + M + G - # indicates high temperature (850°C) and moisture (50% by volume) and gas (50% air, 47.5% N_2 and 2.5% H_2), followed by the displacement rate (mm/s).

	22°C in air	**850°C in air**	**850°C + M + G at 0.09 mm/s**	**850°C + M + G at 0.0009 mm/s**
m	31.7	21.9	27.3	24.6
MoR (MPa)	51.1	70.5	67.9	69.6
Average Stress (MPa)	50.3	68.9	66.6	68.1
Min Stress (MPa)	46.8	63.2	61.1	62.0
Max Stress (MPa)	54.6	76.1	72.4	75.2

The SCG response for the porous tube material was assessed from the strength distributions obtained from testing at 850°C and results are presented in Figure 3.15. The SCG parameters were estimated from this response according to Equation 16 and resulted in a slow crack growth coefficient of 57.9 MPa and the exponent was found to be -218. Overall, these results suggest that the porous MMA tubes exhibit limited SCG sensitivity at 850°C and within the high moisture and gas condition.

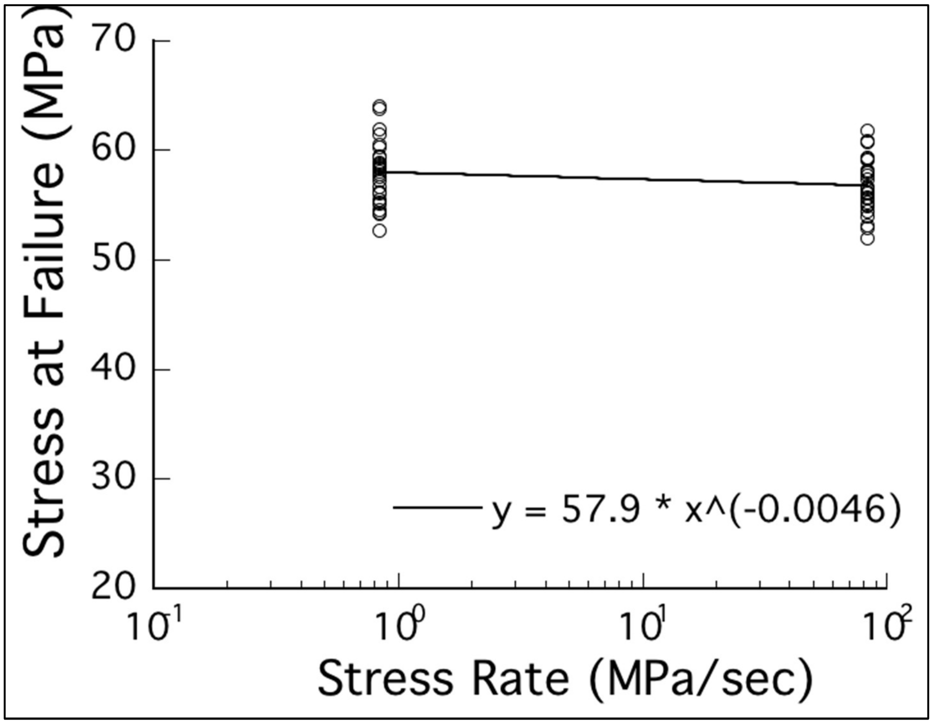

Figure 3.15: Slow crack growth model for the porous MMA tubes tested at 850°C with 50% moisture by volume and mixture of 50% air, 47.5% N_2 and 2.5% H_2. The SCG coefficient and exponent obtained from this analysis are 57.9 MPa and -218.

The previous evaluations involved environmental conditioning, but did not expose the porous materials to elevated temperature and gas over long-term. Therefore, an additional two smaller exploratory evaluations were conducted to see if degradation occurred with longer periods of exposure to the elevated temperature and high moisture level. The first of these tests involved consideration of a crack healing mechanism, which would potentially increase material strength. Tube samples were prepared in the same fashion described in this section and exposed to a temperature of 850°C and moisture content of 50% by volume in surrounding air. Instead of holding these conditions for one hour prior to loading to failure, the samples were exposed to the elevated temperature for 24 hours to allow for slower mechanisms to be revealed. A Weibull plot showing the results of these tests can be seen in Figure 3.16.

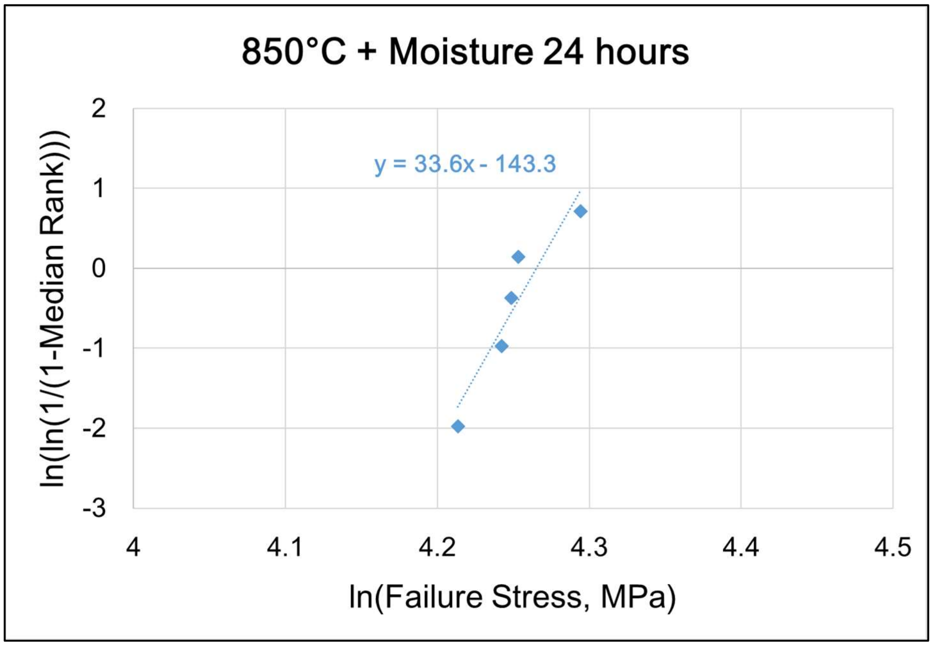

Figure 3.16: Strength distribution of porous MMA tubes after 24-hour exposure to 850°C and 50% moisture by volume in air.

The average strength of the five samples was 70.2 MPa, which agrees very well with results of testing the three groups of MMA tubes at the high temperature as listed in Table 3.2. The only difference to note was an increase in the Weibull modulus, but that could be due to the smaller number of samples tested. More data is needed to verify this trend.

The second set of exploratory tests involved two tube components, one which had not been placed in service, and the other which was placed in operation for many hours and then removed for testing. Specifically, the latter tube was used in an operating fuel cell and underwent typical operating conditions for more than hundreds of hours. Both of the tube components in this evaluation had a thin electrode layer bonded on both sides of the tube. Both components were tested at room temperature and high temperature at a rate of 0.009 mm/sec. Results of this testing are compared in Table 3.3.

Table 3.4: Summary of results comparing the strength of porous MMA tubes that were in service to those which were not.

Not in Service		
	Average Failure Stress (MPa)	Standard Deviation
Room Temperature (22°C)	56.8	1.1
High Temperature (850°C)	68.2	2.0
In Service		
	Average Failure Stress (MPa)	Standard Deviation
Room Temperature (22°C)	53.0	2.0
High Temperature (850°C)	64.3	5.0

The average strength of the tube component that was not placed in service was equivalent to that of the tubes tested under the same conditions and presented in Table 3.2. The strength of the components that saw operation was approximately 4 MPa lower than that of the tubes that did not at both room and high temperature conditions of evaluation. These differences in strength were not statistically significant.

Similar to the fractographic analysis of the fracture surfaces of the dense MMA components, an evaluation of the fractured tube samples was conducted. Particular emphasis was placed on the tensile surface of the specimens where the initiation of failure was most likely. In some specimens that exhibited lower than average stress at failure, one or more visible pores were identified as the origin of fracture. An example of a pore seen from both the tensile surface and the fracture surface is shown in Figure 3.17. When viewed from the fracture surface itself, radial fracture lines can be seen originating from the locations of pores on the tensile surface. Admittedly, the fracture surfaces of the porous tubes were difficult to evaluate due to the large degree of porosity and the corresponding roughness of the fracture surfaces.

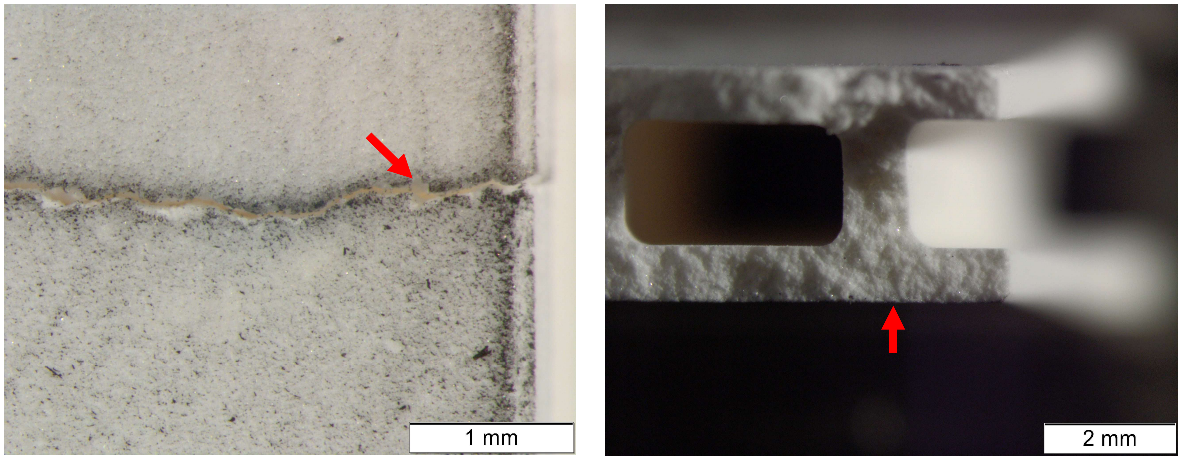

Figure 3.17: Failure origins identified from the fracture surfaces of a porous MMA tube that failed at low stress. Left - View of a pore from the tensile surface along the line of fracture, Right - Markings indicating that fracture initiated from the pore.

3.4 Dense Manifolds

For the dense manifold material of 38% MMA designated as M3, the strength distributions were evaluated at loading rates of 0.00009 and 0.09 mm/s. Results of the testing and the corresponding Weibull models for the two rates of loading are presented in Figure 3.18. The Weibull modulus for samples evaluated at the slower loading rate was 14.4, and was substantially lower than the modulus for the group evaluated at the fastest rate (m=20.3). There was also a 12 MPa reduction in the MoR for the manifolds evaluated at the slowest rate with regards to those evaluated at the fastest rate.

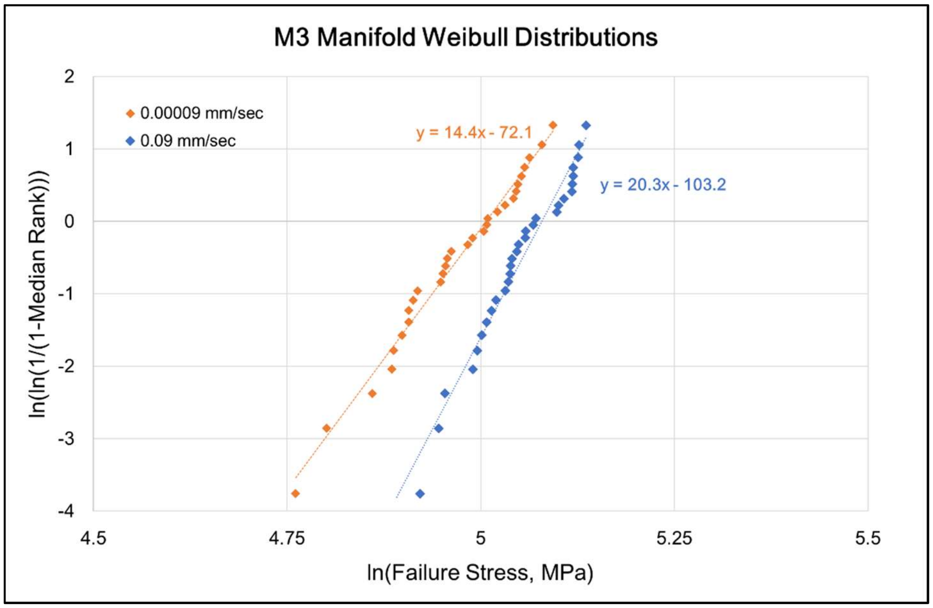

Figure 3.18: Weibull strength distributions for the dense manifold material tested at 50°C and 3.5% moisture by volume in air.

The stress rate dependence of the strength distributions is shown in Figure 3.19. The SCG response of the manifold material was modeled according to Equation 16 through a best fit power law to the strength results. The SCG coefficient was found to be 149 MPa and the SCG exponent was determined to be 82. This value of n indicates that the manifold material has some SCG influence for slower loading rates, but lower than that of the dense endcap components.

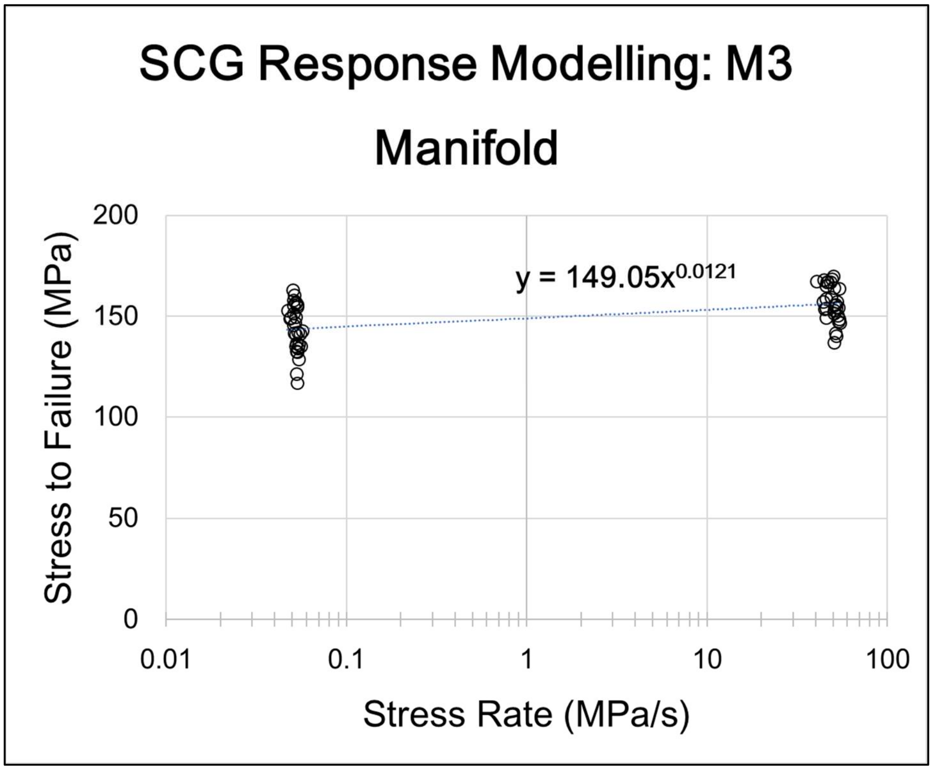

Figure 3.19: Slow crack growth model for the dense manifold material tested at 50°C in air and 3.5° MBV. The SCG coefficient and exponent obtained from this analysis are 149 MPa and 82 MPa.

3.5 Porous YSZ Tape

Consistent with the other fuel cell materials tested, flexure strength distributions were generated for the YSZ tape material according to the conditions outlined in Section 2.5. Results of these experimental evaluations are shown in Figure 3.20, along with the Weibull models for the strength distributions at the two different loading rates. Although there did not appear to be differences in the Weibull modulus with loading rate, the MoR increased with a reduction in the loading rate. The MoR values at the loading rates of 0.09 mm/s and 0.00009 mm/s were 59.6 MPa and 65.7 MPa, respectively. Of note, the Weibull distributions at both loading rates appear to exhibit bimodal behavior, with the highest Weibull moduli exhibited by the lower strength samples of the groups.

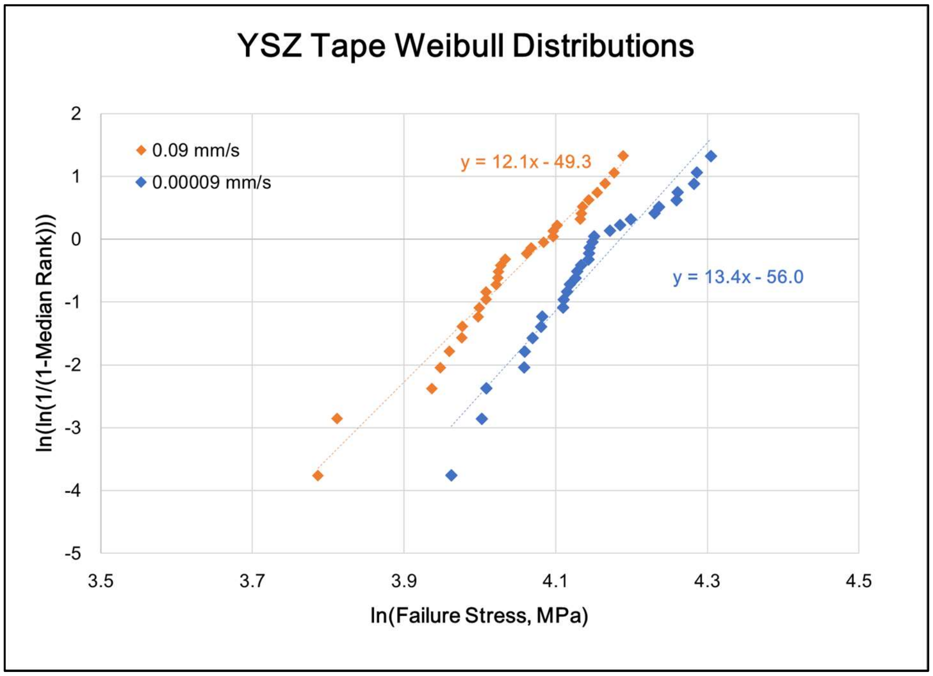

Figure 3.20: Weibull distributions for the YSZ tape tested at 850°C, 50% moisture by volume in an environment consisting of 50% air, 47.5% nitrogen, and 2.5% hydrogen.

The strength distributions for the manifold material and the corresponding SCG model are shown in Figure 3.21. The SCG coefficient and exponent for the manifold material were found to be 58.7 MPa and -67.7 respectively. The small negative SCG exponent suggests that the porous YSZ exhibits reverse SCG sensitivity at 850°C and 50% moisture, indicating that it undergoes an increase in strength with lower stress rate.

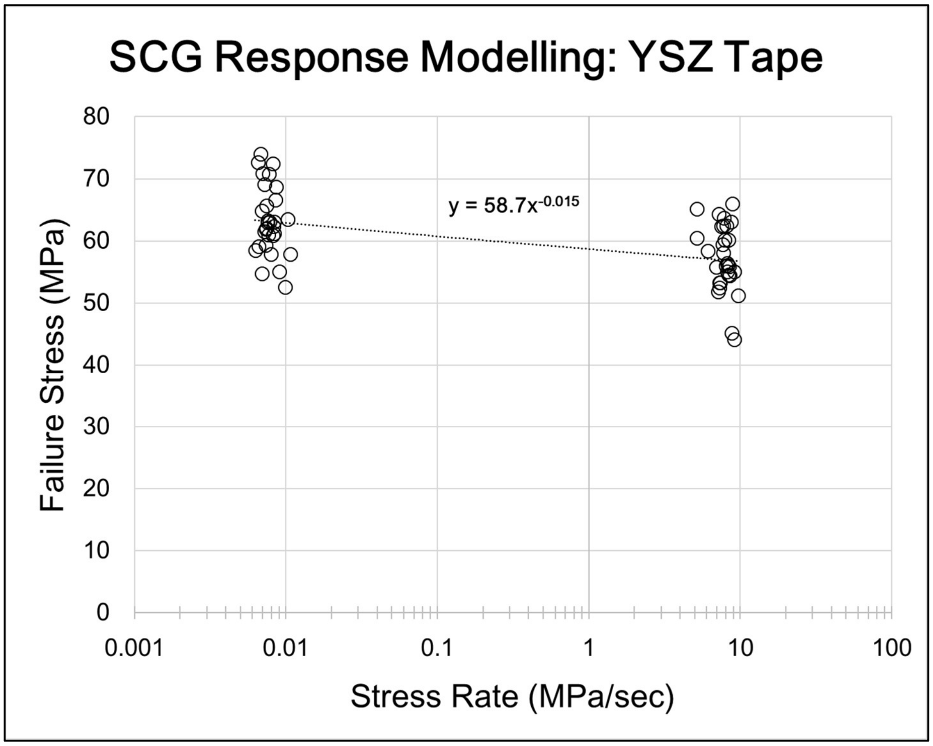

Figure 3.21: SCG model for the YSZ tape material.

The YSZ tape sample surfaces were analyzed under stereomicroscopy to identify any surface features that could contribute to the component failures. The surfaces were generally of high quality and free of defects, although some of the samples did exhibit some large surface pores. Some examples of pores and other markings found can be seen in Figure 3.22. The surfaces in these images have been stained with a highlight marker. Any dark marks are a result of the ink used to highlight defect features and are not indicative of additional materials present.

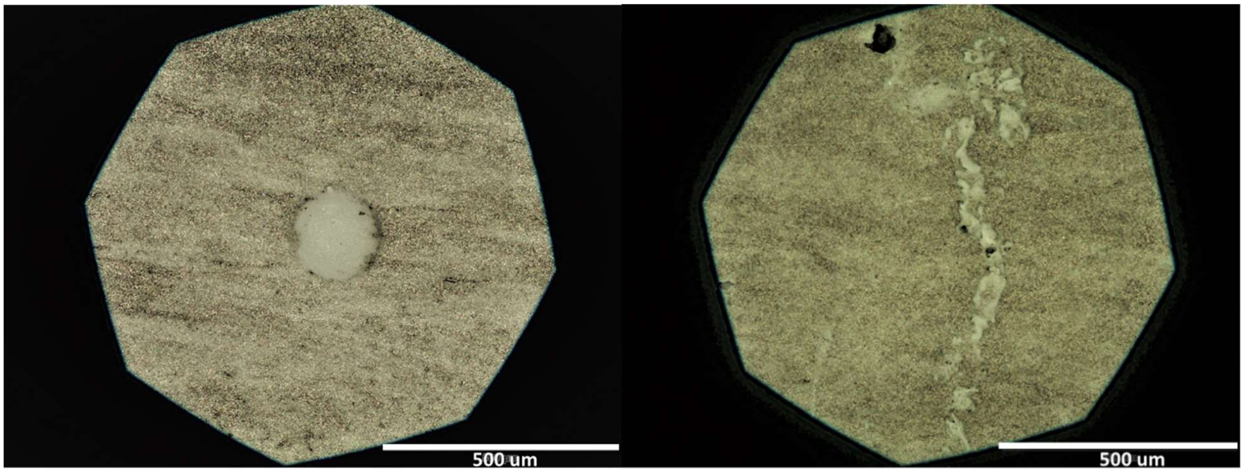

Figure 3.22: Examples of the surface defects on the YSZ tape samples. Left - Pore on the surface of a YSZ sample, Right - Markings left by manufacturing or handling on a YSZ tape sample.

3.6 Fracture Toughness Evaluation

The dense MMA rectangular bars used for the fracture toughness evaluation were polished and then prepared with a central Knoop indentation. Thereafter, the specimens were loaded monotonically to fracture and then the pre-cracks generated by indentation were measured. Due to increased resolution and improved imaging capabilities over optical microscopes, scanning electron microscopy was used to image the pre-cracks at the indentation boundaries after fracture. Each sample was sputter coated before imaging took place to prevent charging and obtain clear images. Although the SEM analysis revealed features that aided in the pre-crack measurement, in several cases it was still difficult to discern the pre-crack geometry. Figure 3.23 contains images of two representative samples where the pre-cracks were identified and provided convenient measurements.

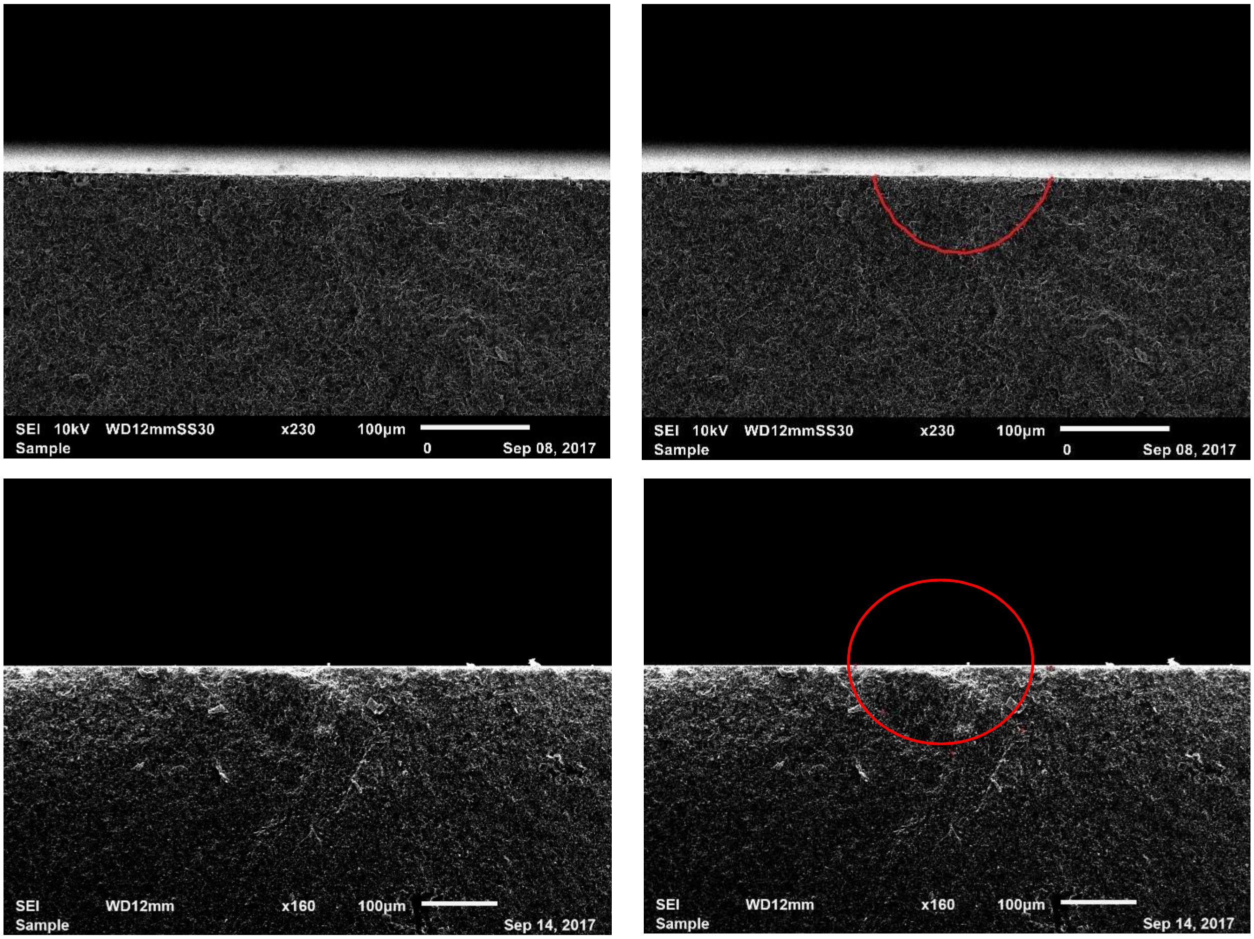

Figure 3.23: Evaluating the initiation flaw lengths for estimating the fracture toughness. Left - Fracture surfaces at the location of the pre-crack (unmarked), Right - Pre-cracks outlined in red.

The average estimated fracture toughness for the dense 38% MMA samples along with standard deviations for each test group are listed in Table 3.4. As evident from these values, the fracture toughness values were consistent regardless of the temperature and distance from the as-manufactured surface. There were no statistically significant differences in the estimated fracture toughness between the four groups.

Table 3.5: Summary of the fracture toughness measurements for the dense 38% MMA material including the average and deviations.

	K_{Ic} (MPa · $m^{1/2}$)	**Deviation**
50°C, Surface	1.81	0.06
850°C, Surface	1.77	0.06
50°C, 250 µm	1.76	0.06
850°C, 250 µm	1.78	0.08

Chapter 4 - Discussion

An experimental evaluation of the microstructure, strength distribution and slow crack growth behavior of candidate solid oxide fuel cell materials was conducted. The evaluation was primarily focused on dense and porous magnesia magnesium aluminate (MMA) materials that are currently being considered as candidates for commercial power systems. The evaluation considered a range of temperatures, levels of moisture and gas environments that are related to the operating conditions and the other conditions that the components may experience from the point of manufacturing to service.

One factor to consider in reviewing the accomplishments and the findings is that the majority of SOFCS are produced from yttria-stabilized zirconia (YSZ) or YSZ hybrids that have been doped with other ceramics [2]. The results presented for the MMA are relatively unprecedented. As such, while providing critical information regarding the durability of these materials and their promise for commercial products, the results of this evaluation also make a contribution to the literature.

4.1 Dense 38% MMA

Results for the first batch of dense 38% MMA materials evaluated were focused on the influence of elevated temperature and moisture on the strength distributions as well as loading rate. According to a comparison of the strength distributions (Figure 3.2) obtained at room temperature in air and at 850°C in air with 3.5% moisture by volume (MBV), the elevated temperature caused a reduction in the strength. The MoR decreased by approximately 10 MPa with increase in temperature (Table 3.1), which represents only 3%. The decrease in strength could be a result of a reduction in surface residual stress with increasing temperature as the surface stress state is compressive [22, 49] and the increase in temperature could promote relaxation in stress with temperature as a result of material expansion. While not validated through measures of residual stress over the range of temperatures evaluated, compressive stresses in ceramics increase their resistance to crack propagation, which would initiate from intrinsic defects in the material.

Another observation from the Weibull distributions for the dense MMA is that the Weibull modulus for the strength distribution obtained at the fastest loading rate was lower than that for the other slower loading rates; the Weibull modulus decreased from an average of approximately 20 to 15. As evident from Figure 3.2, the lower Weibull modulus at 0.09 mm/s loading rate is mainly attributed to the strength of three samples, which exhibited failure stresses that were substantially lower than all of the remaining data points of all the evaluation conditions. The tensile surfaces for these three samples were examined after fracture and large pores were identified as the origins of fracture and were the primary cause for the lower Weibull modulus for this group. Although these three responses may be considered outliers, they do represent the strengths of actual components, and therefore should not be eliminated from the data sets. Clearly, the findings establish that surface porosity is a source for reduced strength of the current generation of MMA components and poses a problem for the reliability of this material as presently manufactured apart from the considerations of slow crack growth. The results also highlight the importance of conducting a statistical analysis of the strength distribution, including the application of the Weibull model. While the majority of samples appear to have consistent failure responses, there are outliers and modifications to the manufacturing process are warranted to better control part quality.

In order for MMA to be effective as a substrate for supporting the fuel cell structure, its mechanical properties should be equal or superior to those of other materials commonly used in fuel cell designs. That statement ignores the economic concern. Comparing the Weibull parameters from Table 3.1 to those in the literature for other fuel cell materials, MMA shows promise as a candidate substrate material. Common cathode materials such as lanthanum strontium manganite (LSM) compositions exhibit a Weibull modulus from as low as 3.7 up to 15 at most depending on the temperatures during evaluation [2]. The MoR for these compositions is also much lower than that of dense 38% MMA at levels ranging from 52 to 138 MPa. Other cathode materials can achieve comparable MoR values, but have Weibull moduli which are over 50% lower than those found for dense 38% MMA [2]. Anode materials such as nickel-based YSZ compositions also show modulus values under 10, showing less reliability compared with the MMA responses [2]. Electrolyte materials tend to have modulus values even lower than those found for common electrode materials with numbers in the range of 3.5 to 9 [2]. The strongest aspect of the MMA revealed in these evaluations is its high consistency and reliability. With modulus values across both dense and porous parts ranging from 15 up to nearly 32, the MMA shows higher reliability than a majority of current fuel cell materials for structural applications. The extended operation of fuel cells requires robust materials that have low probability of failure (high reliability). Based on the results from testing the dense MMA at 850°C, it would be a strong option for use in future cell designs. However, as seen in the differences between two different batches of material from the same manufacturer, material consistency and quality must be standardized so as to ensure predictability.

Results from the rate dependent evaluation of strength and the SCG parameters for the dense 38% MMA were presented in 3.4. According to the power law model for the response, the SCG exponent was found to be -251. The large magnitude indicates that the dense MMA undergoes minimal SCG in the conditions evaluated. Furthermore, the value of n is negative, indicating that the flexure strength increases with reduction in loading rate, which is advantageous for the intended long-term function of the fuel cells. It is generally uncommon for ceramics to exhibit a negative n parameter for SCG. Choi et al. [50] conducted a study on plasma-sprayed ZrO_2 8 WT % Y_2O_3 under constant-stress loading at 800°C. It was found that this particular material was not susceptible to SCG under the tested conditions, and showed a negative response for the SCG exponent. When the magnitude of the SCG exponent is large, there is not a substantial difference in the strength associated with loading rate. If the exponent is small and negative, it is possible that another mechanism is taking place that enhances material strength. Under harsh environments like those explored in this evaluation, it is typical for ceramics to show some decrease in strength as the loading rate is reduced [51]. However, the dense MMA did not.

Complimentary optical and scanning electron microscopic analyses of the dense MMA components showed that they exhibited pores on the surface and within the interior. Although some levels of porosity are to be expected, it was found that there are large voids in the range of 100 μm in size. Interior pores were typically elongated in the plane parallel to the component surfaces (Figure 3.7), which is expected to result from how the material was compacted during manufacturing. Surface pores were identified as the origin of failure for most of those components with comparatively low strength. Clearly, control of porosity should become a priority if component reliability is needed. If outliers can be eliminated, the MMA material will have increased consistency and reliability.

The second batch of dense 38% MMA components received were examined at 50°C and 3.5% moisture owing to concerns of increased SCG sensitivity at this condition. Results of the 4-point flexure experiments showed that the material exhibited differences in the strength distributions from the first batch. The strength distributions were presented in Figure 3.9 and the

Weibull parameters in Table 3.2. As evident in this figure, the second batch of material shows a dominant bimodal response, which was not apparent at either room temperature or at 850°C. The data at each loading rate for the 50°C environment was divided into two groups of responses having unique Weibull moduli, with the largest modulus for the lower strength group. The bimodal response indicates that there are two different mechanisms of failure and/or flaw populations contributing to the failures. One explanation for this behavior is that there are two distinct families of flaws, which result in differing levels of strength and reliability. As shown in the images detailing the component surfaces (Figure 3.11), porosity was more prominent in the second batch of material, relative to the first. Due to larger pores and greater quantities in the second batch of dense MMA components, they would play a larger role on the strength distributions and greater consistency in the low strength failures. The increased porosity content also contributes to the reduction in modulus of rupture due to the stress concentration and greater quantity of material subjected to elevated stress level than the same material with smaller voids. Since both batches of material are from the same manufacturer and are expected to be identical, quality control is a concern. A comparative evaluation of the material behavior is only valuable if the conditions of manufacturing are controlled. It is important to note that for materials which exhibit multiple flaw populations resulting in a bimodal response, more than 30 samples are needed to add accuracy to the strength distribution parameters (i.e. Weibull modulus and MoR) [32].

Although the first batch of MMA components tested at 850°C did not show rate dependence, results for the second batch evaluated at 50°C did indicate that the material is sensitive to SCG (Figure 3.10). According to the power law model, the SCG exponent for the dense MMA was determined to be 29, which is the smallest determined in this investigation. It is a substantial concern. At 50°C and 3.5% MBV, there is a significant reduction in the strength of the dense

MMA with decreasing loading rate. At this temperature level, the slow crack growth mechanisms are activated and cause a reduction to material strength are activated. One factor that may contribute to the bimodal characteristics of the strength distributions at 50°C is an accelerated SCG at the larger surface pores of this second batch of material. Based on the dependence of the mechanisms of degradation on stress, the propensity for SCG is potentially amplified by the aforementioned larger and greater number of surface pores. Indeed, when comparing the bimodal strength distributions at 50°C (Figure 3.9), the degree of bimodality decreases at the lower rate, suggesting that the degradation caused by the larger pores was more severe and uniform. Of course, without further evaluations this is admittedly speculative. Nevertheless, it is critically important to the reliability of the dense MMA components and future work should address this topic in further detail.

It is important to note that the response for the second batch of dense 38% MMA showed the lowest strength and highest SCG sensitivity out of the MMA materials evaluated in this study. Although the full operating temperature that these materials will be exposed to is 850°C, the 50°C condition is important during the manufacturing and assembly of the materials. If the MMA is stored in a heated environment prior to assembly for a prolonged period of time, and this environment has high humidity levels, that could be adequate to promote SCG to initiate from existing defects. As such, the SCG response at this temperature cannot be ignored.

4.2 Porous Tubes

A similar analysis was conducted on the porous 38% MMA tubes at both ambient and elevated temperature (850°C) conditions. The samples evaluated at ambient conditions resulted in the highest Weibull modulus of any material in this study (exceeding m=30 in air), indicating very high consistency in the class of flaws serving as the origins of failure. Interestingly, the porous

MMA underwent an increase in flexure strength with the increase in temperature, and which was true for all three sets of specimens evaluated at the high temperature. In addition, testing a group of samples in air and at 850°C only allowed for more definitive interpretation on how moisture and gas contribute to the strength. In comparing results for the porous tubes tested at 850°C in air, with those tested at 850°C with moisture and gas, it was found that moisture and gas have no significant effect on the strength within the confines of the tests performed. However, it is important to note that the period of testing environment exposure was limited in this study. Although temperature could have an instantaneous influence on the strength, it is possible that prolonged exposure to moisture or the gas could result in a form of aging or degradation which is not seen in the data presented.

Reported studies on the flexure strength of fuel cell ceramics have typically been limited to a small number of variables. The investigation reported by Lowrie and Rawlings [52] explored the response of YSZ materials at room temperature and 950°C. Although they were able to conduct high temperature evaluations, they were not able to successfully test enough samples under those conditions to characterize the strength distribution or perform an evaluation on the SCG response of the material. Other studies were limited in a similar manner where the materials were aged under high temperature conditions with exposure to a hydrogen environment, but the strength tests were only conducted at room temperature or sometimes under high temperature conditions [2]. Moisture has been utilized as a test variable in some cases [53], but it is not typically paired with other operating conditions for fuel cells such as high temperature and a specific gas environment. Hence, the present study is unique in that strength distributions were analyzed based on a consistent and adequate number of samples defined by the ASTM standards, and across a range of conditions. Particularly with the porous MMA tubes, it is possible to see how temperature alone influences the material as well as how moisture and gas contribute to the results. In addition, this study resulted in a unique testing environment where one can control and monitor the moisture and gas contents in real time and modify them as desired. The capacity of this setup is not common and has high potential for future work.

When the porous MMA tubes were exposed to moisture and high temperatures for a 24-hour period, no major changes in the strength were found. This indicates that if moisture has an influence on the tube response, it requires a longer period of exposure to manifest. Due primarily to the cost of the gas mixture used in these studies and the need to focus on other aspects of material performance, the long-term effects of gas exposure were not explored in this investigation. However, an evaluation was conducted on porous tubes that had been in service for a long period of time (t>>1000 hours). By comparing results for the porous MMA that was in-service (Table 3.4) with those not in-service, it was possible to explore the effects of long-term exposure. As described in Section 3.3, the material which had been in service resulted in a reduction in strength of approximately 7%. Nevertheless, these results are from a very limited sample size, and the specimens were obtained from only one tube component. In order to draw a conclusion from this work, more data is required and from multiple components. From all data gathered for the porous tube material, the testing environments considered do not cause a degradation to the strength or reliability of the MMA tubes.

The Weibull modulus for the porous tubes tested at room temperature was quite high (m=31.7) and indicates that the porosity and failure origins were similar from component to component. Although there was an increase in the strength of the porous tubes with increase in temperature to 850°C, there was also a reduction in the Weibull modulus with respect to the ambient data set (Table 3.3); the reduction in m signifies a reduction in the consistency of the strength distributions with increase in temperature. Clearly, this becomes important when constructing structural models that account for cell durability and lifespan. Although an increase in MoR at high temperature is beneficial, the design must be based on the lowest sustainable stress of the MMA over the entire range of operating conditions. As found in evaluations of the dense MMA components, porosity was found to be a contribution to failure of the porous tubes as well. The tubes are processed to have a certain level of porosity, but large pores cause a reduction in strength and can cause outliers in the strength distribution that reduces consistency.

The range of loading rates used in evaluating the MMA tubes enabled a study of strength with respect to stress rate and an evaluation of the slow crack growth sensitivity. Results showed that the average strengths of tests conducted at the 0.09 mm/sec and 0.0009 mm/sec loading rates were statistically equivalent, indicating that that the MMA material does not undergo SCG. Similarly, from a determination of the slow crack growth parameters, the SCG exponent for the tubes is -218, signifying very little rate dependence and that the strength increased with slower loading rates. Therefore, it can be concluded that the porous tubes are not susceptible to SCG mechanisms under the 850°C and high moisture conditions.

4.3 Dense Manifolds

Results of the strength distributions for the MMA manifolds were interesting. As mentioned in Chapter 2, the samples used for testing were taken from two different large manifold components. Samples from each component were tested at both rates and a comparison of the strengths was performed. It was found that at both testing rates, the strengths of samples from one manifold were consistently lower by 5 to nearly 8% (Figure 3.18). These results indicate that there is variability in the component quality between manufacturing runs, and which could promote bias in the evaluation of mechanical properties if steps are not taken to avoid that. Differences in quality could be seen with the naked eye when viewing the cross sections of the manifolds prior to cutting the samples. Specifically, the thickness of the bottom surface varied across the entire width, as well as between vertical material sections. In comparing the two components it was evident that the bottom surface was significantly thinner for one when compared to the other. The thickness of samples from the first component were close to 2 mm, whereas the thickness of samples from the second component were between 1.5 and 1.75 mm. While the differences in thickness did not cause the variations in strength, additional related factors could have contributed to the differences in strength.

The dense manifolds showed some sensitivity to SCG as noted from the 12 MPa reduction in MoR between testing rates, which is over 7% of the total stress to failure. The SCG response and model for the M3 manifold material was presented in Figure 3.19. The SCG exponent for the MMA manifold material is equal to 82, which suggests moderate SCG sensitivity and a reduction in strength with reduction in loading rate. Furthermore, there was reduction in Weibull modulus with decrease in loading rate, which highlights that there was a greater degree of variability in the strength at the lower loading rate. Nevertheless, the influence of SCG is not as prominent as in the second batch of dense 38% MMA.

An SEM analysis was performed on the fractured manifold samples to analyze porosity levels (not shown). It was found that some porosity is present, but at much lower levels than found for the other dense components evaluated in this study. Voids were limited to a size of approximately 50 μm and were sparsely distributed throughout the cross section.

4.4 Porous YSZ Tape

Of all the materials and components evaluated during this investigation, the porous YSZ tape material was the most challenging to test overall. The flexural load to failure was limited by the small tape thickness and porous microstructure of that material. In fact, the upper ceramic loading fixtures contributed a significant percentage of the total load required to initiate failure. In several instances, the YSZ samples broke unexpectedly before flexure loading with the actuator was initiated. This generally happened during the heating phase or when moisture was added into the chamber. When the sample fractured, they consistently broke into many small pieces. Consequently, an analysis of the fracture origin was not possible due to the fixtures crushing the small pieces and obscuring the original fracture surfaces. Some of the early fractures are thought to be a result of air turbulence within the test chamber initiated as moisture was introduced. The flow of water vapor could result in an imbalance of the test fixture. If additional work will be conducted to evaluate the porous YSZ tape or materials with similar thickness and load requirements to fracture, a new fixture design should be considered that reduces the dead weight on the sample.

Based on the Weibull distributions for the YSZ tape, it appears that there are two families of flaws or failure mechanisms that dominated the sample failures. This is seen by the multiple distinct slopes in the distribution of data at each rate (Figure 3.20). According to the optical evaluations of the YSZ sample surfaces, there were two main groups of features that contributed to the failures, including pores and other elongated markings left from manufacturing or handling. One scenario is that the samples with lowest strength had pores on the tensile surface which consistently served as the failure origins. The samples with higher failure strength may have had fewer surface pores, and the other internal or smaller surface defects were then the primary failure origins. In terms of SCG response, the porous YSZ material did not show a degradation in the strength distribution with reduction in the rate of loading (Figure 3.21). In fact, there was an increase in the flexure strength with reduction in loading rate as evident by the negative SCG exponent (n = -67.7).

Yttria stabilized zirconia is a commonly used material for SOFCs. Evaluations of the flexure strength for various YSZ compositions have been performed, but the data available for high temperature evaluations is limited. As the exact composition of the YSZ tape tested in this study is not known, it is difficult to find a direct comparison for the results obtained. In one source with data related to the performance of SOFC materials, there are values listed for the characteristic strength of YSZ at both room temperature (232 MPa) and 800°C (154 MPa) [54]. From this information, it is obvious that high temperature conditions cause a reduction in strength, but both strengths are significantly higher than any obtained in the present study. Additional published data shows Weibull parameters for a Ni-YSZ material under temperatures of 20°C, 600°C and 800°C. The Weibull moduli were in the range of 4.5 to 5.6 with characteristic strengths between 55.4 and 78.9 MPa [55]. In this case, the Weibull moduli are substantially lower than those found in this study, although the characteristic strengths are more consistent with the porous YSZ tested at 850°C. Another group conducted evaluations on YSZ from two manufacturers at room temperature and at 950°C. They also observed a 20-30% reduction in strength from room temperature to high temperature conditions. The resulting Weibull parameters at high temperature in the aforementioned study ranged from 4.5 to 7.3 for the modulus and 205 to 256 MPa for the characteristic strength [52]. Once again, the reported strengths appear to be higher in other studies compared to those found in the present study. It is important to note that this material is porous and the porosity content was not known for this composition. Due to a high dependence of strength on porosity levels [56], it is possible that differences in results could be attributed to higher porosity contents in the materials tested in this study. Nevertheless, according to a review of the literature, testing under simultaneous high temperature and simulated gas environments has not been reported and could have an influence on the strength distributions.

4.5 Fracture Toughness

The evaluation of the dense 38% MMA fracture toughness was initially attempted with 4-point flexure. However, it became apparent that the surface porosity was causing problems as a few samples failed at locations other than the indentation pre-crack. An evaluation of the tensile surface of these samples revealed that there were large pores, some in excess of 200 µm in effective diameter. The measured indentation diagonal length was approximately 215 µm. Surprisingly, the surface pores were large enough, and potentially deep enough, to compete with these indentations in terms of the magnitude of stress intensity. Due to the use of a 4-point bend configuration, any pore located within the inner loading span was subjected to the maximum bending moment and could initiate fracture if that flaw was more critical than the indentation pre-crack. Consequently, it was decided that the 3-point bend configuration should be used to concentrate the bending moment on the indentation pre-crack. After switching from 4-point to 3-point loading, no additional samples fractured at a location other than the intended pre-crack.

The most challenging aspect of the fracture toughness evaluation was measuring the pre-crack sizes. As mentioned previously in Section 3.6, both the color of the material and the rough texture of the fracture surface obscured useful markings that generally help in quantifying the pre-crack dimensions. At first, a stereomicroscope was utilized, but it was nearly impossible to accurately identify and measure pre-cracks on all the samples. Previous studies show that while some ceramics exhibit obvious markings for pre-cracks, others are very challenging to identify [57]. Those groups found that SEM imaging provided additional resolution and the contrast necessary to highlight the important features. In some cases, a semi-circular mark was found for quick measurement of pre-crack size. In others, changes to texture or the presence of velocity hackle lines were used to identify the boundaries of the pre-crack.

The average measured fracture toughness of the MMA using the surface crack in flexure method was approximately 1.78 MPa•m$^{0.5}$. According to the results, there was no significant difference in the fracture toughness measured at 50°C and 850°C. The material did not exhibit any increase in toughness with crack length – that would indicate rising R-curve behavior. In addition, there appears to be no difference in toughness when the pre-crack is located at the surface or within the interior of the sample. These results agree, in general, with those of the flexure testing of the dense MMA, which showed limited influence of temperature.

Results of the fracture toughness measurements using the SENB method were found to be lower than previous results for the dense MMA obtained through indentation hardness testing conducted by LGFCS (2.08 MPa•m$^{0.5}$). Although the hardness testing method for calculating fracture toughness is not standardized and has been the subject of controversy [58], it may be valuable to perform additional tests considering additional locations over the surface of the dense MMA components to see if there are spatial variations in the fracture toughness of this material.

Chapter 5 - Conclusions and Future Work

5.1 Conclusions

An experimental evaluation concerning the microstructure, strength distribution and slow crack growth responses of candidate materials for commercial solid oxide fuel cells (SOFCs) was conducted. The primary materials considered included dense and porous 38% magnesia magnesium aluminate (MMA) and a porous yttrium stabilized zirconia (YSZ) that are used for specific fuel cell components The evaluation considered the materials at ambient and elevated temperatures (50°C and 850°C), with moisture (3.5% and 50%) and within both air and gas (mixture of hydrogen and nitrogen) environments. The strength distributions were characterized by two-parameter Weibull models in terms of the modulus of rupture (MOR) and their Weibull modulus (m). It was determined that slow crack growth did have an effect in some cases, particularly for the dense manifolds and the second batch of dense 38% MMA. Based on the aforementioned work, the following conclusions were drawn:

1. For the dense 38% MMA end caps, results of flexure testing at both ambient conditions and 850°C in air and 3.5% MBV showed that there was limited influence from the increase in temperature. The Weibull modulus and MoR at ambient conditions were 20.7 and 302.2 MPa. At 850°C the average Weibull modulus and MoR were approximately 20 and 290 MPa. Results from the SCG analysis provided a SCG coefficient of D = 281 MPa and an exponent n = -251. At 850°C there is minimal SCG sensitivity.

2. For the dense 38% MMA end caps evaluated at 50°C and 3.5% MBV the average Weibull modulus and MoR were approximately 10 and 190 MPa. The responses were strongly dependent

on the stress rate. Results from the SCG analysis provided a SCG coefficient of D = 147.7 MPa and an exponent n = 29. As evident from that response, the dense MMA exhibits very detrimental SCG sensitivity at the 50°C condition.

3. For the porous 38% MMA tubes, it was found that the increase in temperature from ambient conditions to 850°C resulted in an 18.2 MPa increase to the MoR. The Weibull moduli for sample groups tested under high temperature conditions were lower than that for the ambient sample group. The Weibull modulus and MoR at ambient conditions were 31.7 and 51.1 MPa. At 850°C the average Weibull modulus and MoR were approximately 24.6 and 69.3 MPa. Addition of a gas environment consisting of 50% air, 47.5% N_2 and 2.5% H_2 did not have a visible impact on the strength distributions with respect to tests conducted with high temperature only. Results from the SCG analysis provided a SCG coefficient D = 57.9 MPa and an exponent n = -218. At 850°C with 50% MBV and a mixture of 50% air, 47.5% N_2 and 2.5% H_2, there is minimal SCG sensitivity.

4. For the dense 38% MMA manifolds designated as M3, results of flexure testing at 50°C and 3.5% moisture by volume in air provided a Weibull modulus between 14 and 20 and a MoR of between 150 and 160 MPa. Results from the SCG analysis provided a SCG coefficient of D = 149 MPa and an exponent n = 82. At 50°C there is moderate SCG sensitivity.

5. The overall average fracture toughness of the dense 38% MMA end caps was approximately 1.78 MPa*$m^{0.5}$. There was no difference in the fracture toughness measured at 50°C and 850°C, both at 3.5% MBV, or at the surface and 250 μm below the surface.

6. For the porous YSZ tape it was found that at 850°C, 50% MBV and in a gas environment of 50% air, 47.5% N_2 and 2.5% H_2 that the Weibull modulus was between 12 and 13, and the average MoR was approximately 60 MPa. The slow crack growth evaluations resulted in a SCG exponent of -67.7 and coefficient of 58.7 MPa. This material exhibits reverse SCG sensitivity at this condition, indicating an increase in strength with reduction in stress rate.

7. For all of the materials considered, porosity was found to be a dominant contributor to the initiation of failure and the strength distributions. For future development, consistent control of porosity content and part quality will be key for understanding material durability.

5.2 Future Work

Although the evaluations conducted in this study revealed significant information about the durability of several candidate materials for SOFCs, there is always more to learn to fully understand the materials themselves and how they will behave in the overall fuel cell system. As performed with the first batch of dense 38% MMA and the porous 38% MMA tubes, it would be beneficial to evaluate the room temperature in air responses for the manifolds and the YSZ tape. This would allow for a better understanding of how the operating conditions alter the strength distributions and reliability for those materials. It would also be useful to use a second method to confirm the values obtained for the fracture toughness, for instance using the single-edge notch bend method. With the difficulties in pre-crack measurement and the somewhat small sample size for each condition, obtaining verification would add to the validity of the results. Other tests involving the material's fracture toughness should also be conducted. For example, holding a sample under a set of environmental conditions at a specified percentage of the average fracture toughness would reveal more information about how the materials endure prolonged stress and what level of safety factor is required in operation. The fracture toughness evaluation did not consider SCG because the loading rate was fixed. Future work in this area would be valuable.

The next step to improve the testing setup would be to find a way to directly measure the exact gas composition within the chamber. As it is, the composition is an educated estimate based on real-time readings of moisture content and the known initial gas composition flowing into the chamber. However, to ensure consistency from test to test, having a method to measure the composition of gas would be beneficial.

As mentioned previously, the evaluations within this study mainly considered environmental exposure for short durations of time. Since fuel cell components have characteristically long service lives, conducting additional evaluations on materials which have been in service could be especially valuable in determining the effects of long-term exposure. A design must always conform to the lowest values obtained for a set of environmental conditions under which the material will be exposed to during its service life. If it is determined that properties are reduced after a period of service that is lower than the desired operating life, then the design can be modified ahead of time to avoid those issues. It is hoped that the results of this work and future studies will enable SOFCs to be utilized effectively in the near-future.

Chapter 6 - References

[1] R. M. Ormerod, "Solid oxide fuel cells," *Royal Society of Chemistry,* pp. 17-28, 2002.

[2] A. Nakajo, J. Kuebler, A. Faes, U. F. Vogt, H. J. Schindler, L.-K. Chiang, S. Modena, J. Van herle and T. Hocker, "Compilation of mechanical properties for the structural analysis of solid oxide fuel cell stacks. Constitutive materials of anode-supported cells," *Ceramics International,* vol. 38, no. 5, pp. 3907-3927, 2012.

[3] S. C. Singhal and K. K, High-temperature Solid Oxide Fuel Cells: Fundamentals, Design and Applications, Elsevier Science, 2003.

[4] O. Yamamoto, "Solid oxide fuel cells: fundamental aspects and prospects," *Electrochimica Acta,* vol. 45, no. 15-16, pp. 2423-2435, 2000.

[5] A. B. Stambouli and E. Traversa, "Solid oxide fuel cells (SOFCs): a review of an environmentally clean and efficient source of energy," *Renewable and Sustainable Energy Reviews,* vol. 6, no. 5, pp. 433-455, 2002.

[6] K. C. Wincewicz and J. S. Cooper, "Taxonomies of SOFC material and manufacturing alternatives," *Journal of Power Sources,* pp. 280-296, 2005.

[7] B. Zhu, "Solid oxide fuel cell (SOFC) technical challenges and solutions from nano-aspects," *International Journal of Energy Research,* vol. 33, no. 13, pp. 1126-1137, 2009.

[8] H. Tu and U. Stimming, "Advances, aging mechanisms and lifetime in solid-oxide fuel cells," *Journal of Power Sources,* vol. 127, no. 1-2, pp. 284-293, 2004.

[9] D. P. H. Hasselman, "Thermal stress resistance of engineering ceramics," *Materials Science and Engineering,* vol. 71, pp. 251-264, 1985.

[10] W. D. Kingery, "Factors Affecting Thermal Stress Resistance of Ceramic Materials," *Journal of The American Ceramic Society,* vol. 38, no. 1, pp. 3-15, 1955.

[11] M. Hanasaki, C. Uryu, T. Daio, T. Kawatabata, Y. Tachikawa, S. M. Lyth, Y. Shiratori, S. Taniguchi and K. Sasaki, "SOFC Durability against Standby and Shutdown Cycling," *Journal of The Electrochemical Society,* vol. 161, no. 9, pp. F850-F860, 2014.

[12] G. Robert Humfield Jr. and D. A. Dillard, "Residual Stress Development in Adhesive Joints Subjected to Thermal Cycling," *The Journal of Adhesion,* vol. 65, no. 1-4, pp. 277-306, 1997.

[13] W. T. Chen and C. W. Nelson, "Thermal Stress in Bonded Joints," *IBM Journal of Research and Development,* vol. 23, no. 2, pp. 179-188, 1979.

[14] P. J. Withers, "Residual stress and its role in failure," *Reports on Progress in Physics,* vol. 70, no. 12, pp. 2211-2264, 2007.

[15] B. Eigenmann, B. Scholtes and E. Macherauch, "Determination of residual stresses in ceramics and ceramic-metal composites by X-ray diffraction methods," *Materials Science and Engineering: A,* vol. 118, pp. 1-17, 1989.

[16] V. Hauk, Structural and Residual Stress Analysis by Nondestructive Methods, Amsterdam: Elsevier, 1997.

[17] W. Fischer, J. Malzbender, G. Blass and R. W. Steinbrech, "Residual stresses in planar solid oxide fuel cells," *Journal of Power Sources,* vol. 150, pp. 73-77, 2005.

[18] B. R. Lawn and M. V. Swain, "Microfracture beneath point indentations in brittle solids," *Journal of Materials Science,* vol. 10, no. 1, pp. 113-122, 1975.

[19] H. J. Conrad, W.-J. Seong and I. J. Pesum, "Current ceramic materials and systems with clinical recommendations: A systematic review," *The Journal of Prosthetic Dentistry,* vol. 98, no. 5, pp. 389-404, 2007.

[20] D. J. Green, P. Z. Cai and G. L. Messing, "Residual stresses in alumina-zirconia laminates," *Journal of the European Ceramic Society,* vol. 19, no. 13-14, pp. 2511-2517, 1999.

[21] S. D. Brown, R. B. Biddulph and P. D. Wilcox, "A Strength–Porosity Relation Involving Different Pore Geometry and Orientation," *Journal of the American Ceramic Society,* vol. 47, no. 7, 1964.

[22] M. Oden, "Residual Stress in Ceramics and Ceramic Composites," Linkoping, 1992.

[23] R. Samuel, S. Chandrasekar, T. N. Farris and R. H. Licht, "Effect of Residual Stresses on the Fracture of Ground Ceramics," *Journal of the American Ceramic Society,* vol. 72, no. 10, pp. 1960-1966, 1989.

[24] R. L. Allor and R. R. Baker, "Effect of Grinding Variables on Strength of Hot Pressed Silicon Nitride," *The American Society of Mechanical Engineers,* vol. 5, 1983.

[25] I. Inasaki, "Grinding of Hard and Brittle Ceramics," *CIRP Annals,* vol. 36, no. 2, pp. 463-471, 1987.

[26] D. Munz and T. Fett, Ceramics: Mechanical Properties, Failure Behavior, Materials Selection, Berlin: Springer, 1999.

[27] R. W. Rice, J. J. Mecholsky, S. W. Frieman and S. M. Morey, "Failure Causing Defects in Ceramics: What NDE Should Find," Naval Research Laboratory, Washington, D.C., 1979.

[28] R. Danzer, P. Supancic, J. Pascual and T. Lube, "Fracture statistics of ceramics - Weibull statistics and deviations from Weibull statistics," *Engineering Fracture Mechanics,* vol. 74, no. 18, pp. 2919-2932, 2007.

[29] P. Auerkari, "Mechanical and physical properties of engineering alumina ceramics," Valtion teknillinen tutkimuskeskus, 1996.

[30] G. D. Quinn, "Design Data for Engineering Ceramics: A Review of the Flexure Test," *Journal of the American Ceramic Society,* vol. 74, no. 9, pp. 2037-2066, 1991.

[31] T. Zhang, Q. Zhu, W. L. Huang, Z. Xie and X. Xin, "Stress field and failure probability analysis for the single cell of planar solid oxide fuel cells," *Journal of Power Sources,* vol. 182, no. 2, pp. 540-545, 2008.

[32] ASTM C1161-13, Standard Test Method for Flexural Strength of Advanced Ceramics at Ambient Temperature, ASTM International, West Conshohocken, PA, 2013, www.astm.org.

[33] J. D. Sullivan and P. H. Lauzon, "Experimental probability estimators for Weibull plots," *Journal of Materials Science Letters,* vol. 5, no. 12, pp. 1245-1247, 1986.

[34] S. F. Duffy, "Weibull Parameter Estimation: Theory and Background Information," Connecticut Reserve Technologies, Cleveland, 1997.

[35] C. C. Gonzaga, P. F. Cesar, W. G. J. Miranda and H. N. Yashimura, "Slow crack growth and reliability of dental ceramics," *Dental Materials,* vol. 27, no. 4, pp. 394-406, 2011.

[36] R. J. Charles, "Dynamic Fatigue of Glass," *Journal of Applied Physics,* vol. 29, no. 12, 1958.

[37] S. M. Wiederhorn and L. H. Bolz, "Stress Corrosion and Static Fatigue of Glass," *Journal of The American Ceramic Society,* vol. 53, no. 10, pp. 543-548, 1970.

[38] A. G. Evans, "Slow crack growth in brittle materials under dynamic loading conditions," *International Journal of Fracture,* vol. 10, no. 2, pp. 251-259, 1974.

[39] N. J. v. d. Laag, Environmental effects on the fracture of oxide ceramics, 2002.

[40] T. Okabe, M. Kido and T. Miyahara, "Fatigue fracture behavior of oxide ceramics in water," *Engineering Fracture Mechanics,* vol. 48, no. 1, pp. 137-146, 1994.

[41] R. W. Rice, "Slow crack growth in MgAl2O4 single- and poly-crystals," *Journal of Materials Science Letters,* vol. 14, pp. 723-727, 1995.

[42] M. Ciccotti, "Stress-corrosion mechanisms in silicate glasses," *Journal of Applied Physics D: Applid Physics,* vol. 42, no. 21, 2009.

[43] J. E. Ritter Jr and C. L. Sherburne, "Dynamic and Static Fatigue of Silicate Glasses," *Journal of the American Ceramic Society,* vol. 54, no. 12, pp. 601-605, 1971.

[44] ASTM C1368-10(2017), Standard Test Method for Determination of Slow Crack Growth Parameters of Advanced Ceramics by Constant Stress-Rate Strength Testing at Ambient Temperature, ASTM International, West Conshohocken, PA, 2017, www.astm.org.

[45] E. Yalamac, "Effect of Spinel Addition on the Sintering Behavior and Microstructure of Alumina-Spinel Ceramics," *Ceramics-Silikaty,* 2014.

[46] ASTM C1421-16, Standard Test Methods for Determination of Fracture Toughness of Advanced Ceramics at Ambient Temperature, ASTM International, West Conshohocken, PA, 2016, www.astm.org.

[47] B. Bergman, "On the estimation of the Weibull modulus," *Journal of Materials Science Letters,* vol. 3, no. 8, pp. 689-692, 1984.

[48] B. Faucher and W. R. Tyson, "On the determination of Weibull parameters," *Journal of Materials Science Letters,* vol. 7, no. 11, pp. 1199-1203, 1988.

[49] J. Malzbender, W. Fisher and R. W. Steinbrech, "Studies of residual stresses in planar solid oxide fuel cells," *Journal of Power Sources,* vol. 182, no. 2, pp. 594-598, 2008.

[50] S. R. Choi, D. Zhu and A. R. Miller, "High-Temperature Slow Crack Growth, Fracture Toughness and Room-Temperature Deformation Behavior of Plasma-Sprayed ZrO2-8 WT % Y2O3," *Ceramic Engineering and Science,* vol. 19, no. 4, p. 293, 1998.

[51] R. W. Davidge, J. R. McLaren and G. Tappin, "Strength-probability-time (SPT) relationships in ceramics," *Journal of Materials Science,* vol. 8, no. 12, pp. 1699-1705, 1973.

[52] F. L. Lowrie and R. D. Rawlings, "Room and high temperature failure mechanisms in solid oxide fuel cell electrolytes," *Journal of the European Ceramic Society,* vol. 20, pp. 751-760, 2000.

[53] G. Bansal and W. H. Duckworth, "Effects of moisture-assisted slow crack growth on ceramic strength," *Journal of Materials Science,* vol. 13, pp. 239-242, 1978.

[54] J. T. S. Irvine and P. Connor, Solid Oxide Fuel Cells: Facts and Figures, Springer Science & Business Media, 2012.

[55] T. Ohji and M. Singh, Engineered Ceramics: Current Status and Future Prospects, John Wiley & Sons, 2016.

[56] M. Radovic and E. Lara-Curzio, "Mechanical properties of tape cast nickel-based anode materials for solid oxide fuel cells before and after reduction in hydrogen," *Acta Materialia,* vol. 52, no. 20, pp. 5747-5756, 2004.

[57] G. D. Quinn, J. J. Kubler and R. J. Gettings, "Fracture Toughness of Advanced Ceramics by the Surface Crack in Flexure (SCF) Method: A VAMAS Round Robin," John Wiley & Sons, Inc., 1994.

[58] G. D. Quinn and R. C. Bradt, "On the Vickers Indentation Fracture Toughness Test," *Journal of the American Ceramic Society,* vol. 90, no. 3, pp. 673-680, 2007.

[59] "Compilation of mechanical properties for the structural analysis of solid oxide fuel cell stacks. Constitutive materials of anode-supported cells," *Ceramics International,* vol. 38, pp. 3907-3927, 2012.